A novel 3D PDAC model system developed with the use of decellularized matrix scaffolds

By

Ezekiel Rozmus

This thesis is submitted in partial fulfillment of the requirements for the degree of Master of Science in Biomedical Sciences

Department of Biomedicine/Klinisk Institutt 2
University of Bergen
June 2019

Acknowledgements

The study performed in this thesis was carried out at Klinisk Institutt 2 at Haukeland University Hospital, with the support of the Department of Biomedicine at the University of Bergen from the period of January 2018 to June 2019.

Firstly, I would like to express my gratitude to my supervisor, Emmet Mc Cormack, for his excellent guidance, always being available to answer questions, and always encouraging me forward with his guidance. I would also like to extend my thanks to my co-supervisor, Gorka Ruiz de Garibay, for his wonderful and consistent advice and assistance.

I would also like to thank the entire Mc Cormack group for everyone's willingness to help. It truly was a wonderful working environment. Especially, I would like to thank Anika Langer, who, alongside my supervisors, provided invaluable assistance throughout my time working on this thesis. I would also like to extend my thanks to Spiros Kotopoulis, who was a wonderful resource for general advice as well as his assistance in the model design and printing process.

Furthermore, I would like to thank Hege Avsnes Dale and all those at the Molecular Imaging Center at the University of Bergen, for their assistance in my training in all aspects of image acquisition and analysis. I would also like to express my gratitude to Brith Bergum for her assistance in cell sorting and advice regarding flow cytometry. I would also like to thank Anders Molven for his contributions in PDAC material as well as advice in carrying out histology experiments.

Finally, I would like to thank my family and friends, both those continuing to support me while I am far from home and those here with me in Norway.

Bergen, June 2019

Ezekiel Rozmus

Table of Contents

Acknowledgements ..... **i**
Table of Contents ..... **ii**
Abbreviations ..... **v**
Summary ..... **vii**
1 Introduction **1**
1.1 Pancreatic Ductal Adenocarcinoma 1
1.1.1 Biology and development of PDAC *1*
1.1.2 Current PDAC therapy *1*
1.2 PDAC Stroma 2
1.2.1 Cellular stromal components *3*
1.2.2 Non-cellular stromal components *3*
1.3 Pre-Clinical Models 4
1.3.1 Patient-derived cell lines *4*
1.3.2 Patient-derived xenograft models *5*
1.3.3 3D cell culture models *6*
1.3.4 Development of 3D matrix materials *7*
1.3.5 3D models developed with decellularized matrix scaffolds *8*
1.4 Optical imaging modalities 9
1.4.1 Confocal Microscopy *9*
1.4.2 Fluorescent reporter genes *10*
1.4.3 Imaging unlabeled cell lines *10*
2 Aims **12**
3 Materials and Methods **13**
3.1 Cell Experiments 13
3.1.1 Cell Culture *13*
3.1.2 Freezing of Cells *14*
3.1.3 Thawing of Cells *14*
3.2 Viral transduction of BJ fibroblasts 14
3.2.1 Production of virus *14*

3.2.2 Transduction of BJ fibroblasts *15*
3.2.3 Preparation of cells for flow cytometry *15*
3.2.4 Preparation of cells for sorting with FACS *16*
3.2.5 Confirmation and selection of NTR positive cells *16*
3.3 SISser scaffold system preparation 17
3.3.1 Cell crown production *17*
3.3.2 WST-1 toxicity assay *17*
3.3.3 Production of SISser matrices *18*
3.3.4 Mounting of decellularized matrix *19*
3.3.5 Cell seeding and culturing on scaffolds *19*
3.3.6 Preparing scaffold system for imaging *19*
3.3.7 Assessment of matrix permeability *20*
3.4 Confocal Microscopy 21
3.4.1 Image acquisition *21*
3.4.2 Image processing *22*
3.5 Histology 22
3.5.1 Fixation and embedding of scaffolds *22*
3.5.2 Slicing of histology samples *23*
3.5.3 Hematoxylin-Eosin (H&E) staining *23*
3.5.4 Masson-Goldner Trichrome staining *24*
3.5.5 Slide Imaging *24*
3.6 Statistics 24
4 Results 25
4.1Optimization and validation of the 3D culture system 25
4.1.1 Cell crown design *25*
4.1.2 WST-1 Toxicity Assay *26*
4.1.3 Assessment of scaffold permeability *28*
4.1.4 "In-house" production of SISser *28*
4.1.5 Assessing imaging potential of the system *28*
4.1.6 Optimization of Calcein-AM fluorescent dye *29*
4.1.5 Accuracy of Calcein-AM signal *29*

4.2 Pancreatic cell growth in monoculture 31
4.2.1 MIA PaCa-2 monoculture 31
4.2.2 BxPC-3 monoculture 31
4.2.3 PANC-1 monoculture 32
4.2.4 Quantification of monoculture fluorescent signals 33
4.3 Preparation for coculture experiments 35
4.4 Pancreatic cell growth in coculture with BJ fibroblasts 36
4.4.3 MIA PaCa-2 + BJ Fibroblasts 36
4.4.2 BxPC-3 + BJ Fibroblasts 37
4.4.3 PANC-1 + BJ Fibroblasts 38
4.4.4 Quantification of culture fluorescent signals 38
4.4.5 BJ Fibroblasts in coculture 41
4.5 Comparison with established model systems 42
5 Discussion 44
5.1 Optimization and validation of the 3D culture system 44
5.2 Pancreatic cell growth in monoculture 46
5.3 Preparation for coculture experiments 47
5.4 Pancreatic cell growth in coculture with BJ fibroblasts 48
5.5 Comparison with established model systems 49
5.6 Future perspectives 50
References 53

Abbreviations

BSA	Bovine serum albumin
CAF	Cancer associated fibroblast
CLSM	Confocal laser scanning microscopy
CTGF	Connective tissue growth factor
DMEM	Dulbecco's Modified Eagle Medium
DMSO	Dimethyl sulfoxide
DNase	Deoxyribonuclease
DOC	Sodium deoxycholate
DPX	Distyrene, tricresyl phosphate, and xylene
DSMZ	Deutsche Sammlung von Microorganismen und Zellkulturen (The German Resource Center for Biological Material)
ECM	Extracellular matrix
EMT	Endothelial to mesenchymal transition
FACS	Fluorescence-activated cell sorting
FBS	Fetal bovine serum
FSC	Forward scatter
GFP	Green fluorescent protein
H&E	Hematoxylin-Eosin
HA	Hyaloranin
HBSS	Hank's Balanced Salt Solution
HeBS	Hepes-buffered saline
HS	Horse serum
IPMN	Intraductal papillary mucinous neoplasms
L-G	L-Glutamine
MUC	Mucosa
NTR	Nitroreductase
P/S	Penicillin/Streptomycin
PanIN	Pancreatic intraepithelial neoplasia
PBS	Phosphate-buffered saline
PCL	Polycaprolacetone
PDAC	Pancreatic ductal adenocarcinoma
PDGF	Platelet-derived growth factor
PDX	Patient-derived xenograft
PEEK	Polyether ether ketone
PFA	Paraformaldehyde
PSC	Pancreatic stellate cell
RHAMM	HA-mediated motility receptor
RPMI	Roswell Park Memorial Institute

SDCLM	Spinning disk confocal laser microscopy
SER	Serosa
SIS	Submucosa
SISser	Decellularized matrix containing submucosa and serosa layers
SSC	Side scatter
TU	Transducing Units

Summary

The tumor microenvironment consists of a complex system of interactions, with multiple cell types such as fibroblasts, macrophages, and endothelial cells present alongside cancer cells. This microenvironment is especially important in Pancreatic Ductal Adenocarcinoma (PDAC), as the interaction between PDAC tumor cells and the surrounding microenvironment has been shown to play a significant role in the development and progression of PDAC, as well as the inhibition of targeted therapeutic strategies. Therefore, any preclinical model systems attempting to replicate PDAC for the analysis and development of therapeutic strategies must include or address this microenvironment in some manner.

In this study, we have designed and applied a novel PDAC model system with the use of decellularized porcine intestine, with the potential to reflect the complex tumor-stroma interactions seen in PDAC. A framework for the model was developed to allow for the real-time visualization of cells so that experimental efficiency and reliability may be maximized through implementation of dynamic endpoints. Furthermore, the growth and development of PDAC cells was analyzed within the system both alone and in coculture alongside fibroblasts, to assess development and interactions between the two cell lines.

Multiple cell lines were able to be grown, retaining distinct growth patterns. Interactions between fibroblasts and pancreatic cells were also observed, with fibroblast addition generally correlating with increased cell proliferation. An imaging system was successfully developed allowing the following of multiple cell lines concurrently. Comparisons of our preliminary system with other established preclinical models shows promise in the potential for biological relevance.

1 Introduction

1.1 Pancreatic Ductal Adenocarcinoma

Pancreatic Ductal Adenocarcinoma (PDAC) has an overall five-year survival rate of only 9%, with the incidence of death rates increasing from 2012-2016 (1). PDAC is diagnosed at a median age of 70, and its presentation is typically characterized by late-stage detection (2). This delay between onset and diagnosis is generally attributed to the high mortality rates and low treatment efficacy seen in PDAC patients (3).

1.1.1 Biology and development of PDAC

PDAC develops in the ductal epithelium of the pancreas, forming from non-malignant precursor lesions (4). Common precursor lesions include intraductal papillary mucinous neoplasms (IPMNs), and pancreatic intraepithelial neoplasia (PanIN) (5). Of the two, PanIN is much more prevalent, with well-established classifications (6,7). During the development of PDAC from pre-malignant precursor lesions to an advanced stage invasive cancer, the mutated cells will spend many years confined to the pancreas before adopting a metastatic phenotype (8). However, once the disease progresses to a more advanced stage, rapid progression is observed, putting additional strain on treatment efficacy (9).

Approximately 10% of PDAC cases arise from familial origins (10), with the majority of incidences arising from sporadic development (2). There are genetic commonalities in PDAC, with each typically containing one or more common mutations (11). The more prevalent abnormalities are the activation of KRAS and inactivation of *CDKN2A*, each seen in approximately 90% of PDAC cases. Other mutations commonly present include the inactivation of *TP53*, as well as the inactivation of *DPC4* (11).

1.1.2 Current PDAC therapy

Out of the cases of PDACs that are successfully diagnosed, less than 20% are resectable (12), putting an emphasis on the need for non-surgical treatment options. In patients with non-resectable PDAC, the disease has commonly progressed to a metastatic state. However, tumors that involve the celiac axis or superior mesenteric artery of the pancreas are also considered non-resectable, even when they have not spread beyond the pancreas (13). Due to the difficulty in

surgical intervention, PDAC treatment has historically been characterized by chemotherapy. Initially this involved solely the administration of gemcitabine, increasing the median survival by approximately 5.6 months (14). Recently, other therapeutic standards have come into practice. FOLFIRINOX, a combination of oxaliplatin, irinotecan, fleurouracil, and leucovorin, was introduced as an alternative to monotherapy with gemcitabine, demonstrating an overall survival of 11.1 months (15). Compared to gemcitabine however, FOLFIRINOX has a more hazardous safety profile, correlating with higher incidences of fibrotic neutropenia, thrombocytopenia, diarrhea, sensory neuropathy, and alopecia (15). As an alternative to FOLFIRINOX, albumin-bound paclitaxel (nab-paclitaxel) combined with gemcitabine has been associated with an overall survival of 8.5 months. There is not an increase in secondary effects seen in nab-paclitaxel + gemcitabine administration compared with gemcitabine alone, although there are occasional cases of peripheral neuropathy which can be rapidly reversed (16). Current standards of care for non-resectable PDAC include both FOLFIRINOX and nab-paclitaxel + gemcitabine, with FOLFIRINOX primarily administered to patients with good performance status, and nab-paclitaxel + gemcitabine administered to a more broad patient cohort less suited for the toxicity of FOLFIRINOX (17).

1.2 PDAC Stroma

One reason why there has been much difficulty in providing effective therapies for PDAC is the stroma (18). PDAC is characterized by a highly desmoplastic and fibrotic tumor microenvironment, with an increased ratio of stromal factors and components compared to the pancreatic cancer cells themselves (19). There are many components in this stromal environment, the most prominent of which include cancer-associated fibroblasts (CAFs) and immune cells (20). These components of the stroma interact with the cancer cells and drive the stimulation of many extracellular matrix (ECM) factors, such as fibronectin, collagen I, hyaloranin, laminin, as well as various growth factors including connective tissue growth factor (CTGF), platelet-derived growth factor (PDGF), and transforming growth factor-beta (TGF-β) (21, 22).

1.2.1 Cellular stromal components

In the stroma, fibroblasts play a large role in creating the complex, desmoplastic environment commonly seen in PDAC. Pancreatic stellate cells (PSCs) are the most common and prolific cell within PDAC stroma (23). In cancerous tissue, PSCs are activated through the increased signaling from nearby cancer cells, at which point they begin to develop a myofibroblast-like phenotype (24). These activated cells then produce a number of ECM components, as well as growth factors that serve as a positive feedback loop, further increasing the number of activated PSCs and ECM material (24). The increased concentration of PSCs seen in PDAC has been shown to be correlated with an increase in growth and metastasis in orthotopic models (25). Activated PSCs also have an effect on the pancreatic cancer cells, inducing an increased proliferation rate as well as resisting apoptotic signals (24). These effects are reversible, as inactivation of these PSCs is attributed to a more favorable tumor microenvironment, slowing progression of tumor development (26).

Along with PSCs, immune cells such as macrophages play a large role in defining the characteristics of the PDAC tumor environment. Traditionally, there are two types of activation that a macrophage can undergo, M1 and M2 activation. M1 activation denotes a classically activated macrophage, and these cells typically serve the function of protecting against pathogens. M2 activated macrophages, however, are activated through alternative, non-classical pathways, and have been shown to correspond with tumor progression (27). The macrophages found in PDAC have been shown to correspond with the alternatively activated M2 phenotype (28). The macrophages found surrounding PDAC tumors drive its progression by increasing the proliferation of pancreatic cancer cells and facilitating cell migration, as well as acting in a positive feedback loop by further recruitment of other immune cells (28).

1.2.2 Non-cellular stromal components

The most commonly present non-cellular ECM factor found in PDAC stroma is type I collagen (29). Type I collagen is known to inhibit the ability of cancer cells to invade by forming a barrier which will impede movement of cells (30). However, type I collagen has conversely been shown to promote cancer cell invasion through the induction of endothelial to mesenchymal transition (EMT), in which cancer cells adopt a more mesenchymal phenotype allowing them to invade and

migrate through tissue (30). This conflicting role of type I collagen can be attributed to multiple isoforms created under differing conditions (29). The normal isoform of type I collagen produced by CAFs and other fibroblasts are known to be heterotrimers, while in cancerous tissue homotrimers are synthesized by the cancer cells themselves as a means of promoting EMT and invasion (29).

Hyaloranin (HA) is an ECM component commonly overproduced in the PDAC stroma, where its function is to gather and form around cells, creating a matrix capable of signal transduction surrounding the cancer cells (31). The most common receptor targets of HA include CD44 and the HA-mediated motility receptor (RHAMM) (32). Another common ECM component is laminin, often involved as a factor essential for cell adhesion, differentiation, and migration (35). Increased expression of both HA and laminin is correlated with accelerated tumor progression, as well as poor survival in PDAC patients (33, 34, 35).

Multiple growth factors are overexpressed in the stroma of PDAC, including CTGF, PDGF, and TGF-β (36). These growth factors are commonly attributed to driving the development of the highly desmoplastic microenvironment by instigating the production of stromal components as well as large amounts of connective tissue, ultimately leading to a growth advantage for the tumor tissue (19, 37).

1.3 Pre-Clinical Models

1.3.1 Patient-derived cell lines

To allow for a better understanding of the complex microenvironment present in PDA, the development of accurate pre-clinical models is vital for progress in characterization and treatment. Perhaps the most fundamental method of modelling PDAC is through the culturing and study of pancreatic cancer cells derived from patient material. These cells are harvested from either the primary tumor sites or from distant metastases, resulting in a collection of immortalized cancer cells that can be expanded and characterized (38). Patient-derived cell lines are useful for efficient characterization and identification of possible target pathways for therapy due to their quick and consistent growth, as well as the availability of efficient screening methods such as high-throughput RNAi, which can analyze a large number of target genes in a

short period of time (39). The migratory activity and invasion potential of pancreatic cell lines may be analyzed through the application of wound-healing and transwell assays, respectively (40, 41). These cell lines may also be used in drug screening when testing novel therapies (42). Using the results from the characterization and classification of pancreatic cell lines, subtypes of PDAC were identified, allowing patients to be segmented into effective therapy groups based on the characteristics of their disease (43).

However, while patient-derived cell lines have proven quite useful in the identification and classification of many instances of PDAC, the potential for this system to be used as a pre-clinical model is limited. Perhaps the most significant factor preventing pancreatic cell lines alone from accurately reflecting PDAC as it occurs in patients is that, when cultured, the system typically consists of a 2D monolayer of cells growing across a plastic surface. This system lacks the structural framework and support seen *in vivo*, as well as all mechanical context provided by the stroma and areas surrounding the tumor (44). Also, due to the fact that patient-derived cell lines consist solely of cancer cells, there is a lack of a representative microenvironment, which ignores the effects of the complex interactions seen within the stroma and ECM (45).

1.3.2 Patient-derived xenograft models

In an attempt to more accurately reflect the complex microenvironment that contributes to tumor growth and development, the patient-derived xenograft (PDX) model system was developed. In this system, tumor samples from the patient may be engrafted into immunocompromised mice either as solid tumor pieces, or a cell suspension created through the digestion and processing of these tumor pieces (46). While solid tumor engraftments often have difficulties in growing successfully, they have been shown to more accurately represent drug response than other engraftment methods, such as traditional cell line-derived xenograft models (47).

The most apparent benefit to PDX models is that the system allows for patient samples to be grown and developed in an *in vivo* environment that much more closely represents the 3D nature seen in the patient, especially when compared to a 2D system *in vitro* (48). Similarly to patient-derived cell lines, xenograft models provide the opportunity for characterization of patient material. However, these xenograft models are useful for discovering more accurate biomarkers

that may not be present without the three-dimensional structure and interaction of the microenvironment (49). This in turn creates a more accurate overview of the characteristics seen in an individual patient, which leads to the potential for better personalized treatment (50). Also, due to their ability to more accurately portray drug response than other systems, xenograft models have been used in generalized studies as a means of testing drug efficacy (51, 52).

However, while PDX models provide a beneficial utility and have proven useful in preclinical studies, the system still has some limitations. For example, not every patient sample can be successfully engrafted and grown even in immunocompromised mice, and samples that are able to grow successfully actually serve as a predictor for poor prognosis (49). This means that less aggressive tumors may not be represented, skewing the availability of the model towards more aggressive tumors. When gathering patient material, many aggressive cases of PDAC are diagnosed at a non-operable stage (53), though techniques such as fine needle aspirate biopsies may be used to retrieve tumor samples (54). Even when a sample is successfully engrafted, there is a significant time of development within the mouse before the model can be used. This delay between the time of implantation and successful development can take longer than 4 months for each sample (55). Considering the correlation between successful engraftment and tumor aggression, this delay is especially dangerous. Xenograft models also rely on the development of mouse stroma surrounding the transplanted patient material, and this drift from human to mouse stroma adds some limitations such as potentially inaccurate tumor-stroma interaction, as well as a lack of inflammatory cells present in PDAC patients (56).

1.3.3 3D cell culture models

While *in vivo* models provide a biologically representative model and environment, their limitations demonstrate a need for more efficient *in vitro* models that can approach the accuracy seen *in vivo* while retaining the time and cost effective properties of traditional *in vitro* systems. One such model is the spheroid model, in which cells are cultured in suspension using a matrix most commonly composed of Matrigel or collagen along with the appropriate growth factors (57). While suspended, the cells are able to grow in three dimensions, resulting in the development of a cluster of cells in contrast with the monolayer seen in 2D cultures.

The 3D structure of this model system also has the potential to maintain structural morphology. This is demonstrated in PDAC models in which much of the ductal cell morphology is retained after culturing the cells *in vitro* (58, 59). Along with a more accurate structural model, spheroid models also display expression patterns more similar to those seen *in vivo*. For example, 3D cultures of PDAC cells exhibited increased expression of ECM components, as well as a shift to the more glycolytic metabolism seen in PDAC tumors when compared with their 2D counterparts (60).

Patient material can be resected and implemented into a 3D culture system where it can be grown and characterized much more quickly than *in vivo* models, providing information about the patient in a much more reasonable time frame (58). Also, drug screening can be performed on organoids developed from patient material, allowing treatment to be personalized for each patient (61).

1.3.4 Development of 3D matrix materials

Much progress is being made as well in the development of biologically accurate matrices in which cells can be cultured. One way in which these 3D models have become more relevant is through adapting many of the mechanical properties of the ECM to more accurately reflect what is present natively. ECM stiffness is an important factor of the cellular environment affecting cell growth and development (62), influencing cell morphology and migrational ability (63). Synthetic hydrogels have been developed with the ability to manipulate the stiffness of the simulated ECM, demonstrating the ability to assess the development of cells under a variety of structural conditions (64). Synthesized materials, such as polycaprolacetone (PCL) are also available as printed discs containing micropores that provide a structural scaffold to analyze cell-ECM interactions (65).

Given the significance of cell interaction with the ECM, it is important in a 3D model system that the composition of the matrix in which the cells are grown accurately reflects the natural environment. There is a great variety in ECM expression patterns and signaling interactions with cells seen *in vivo* (66), which provides some difficulties in the development of a generic and

widely-applicable matrix material. To address this, modifiable hydrogels are available with the potential to be manufactured with varying composition of ECM components, such as collagen I, collagen IV, fibronectin, and laminin (67). The versatility of these hydrogels allow for the development of a 3D model system specialized for accurate ECM interactions with many cell types.

1.3.5 3D models developed with decellularized matrix scaffolds

When developing a pre-clinical model system, the type of matrix on which pancreatic cells are grown is responsible for providing an environment with the potential for accurate growth and interaction of the constituents within the system. With the use of Matrigel, cells may certainly grow into 3D structures; however, each of these structures is largely independent of those surrounding it and the complex system of stroma-tumor interactions remain ignored. Using a more biologically relevant scaffold on which the cells may grow can address some of these issues. One solution is through the use of decellularized porcine intestine, which can be divided into the mucosa (MUC), submucosa (SIS), and serosa (SER) layers (68). Cells may be seeded and grown on these surfaces to analyze their morphological growth and expression patterns (69).

When manufactured, these scaffolds undergo a decellularization process that removes cellular material and DNA residue while preserving the ECM, resulting in a biologically accurate scaffold composed primarily of collagen and elastin fibers (70, 71). When cultured on these scaffolds, multiple cell types develop in a more biologically relevant manner as opposed to other *in vitro* models. Hepatic cells seeded on a decellularized scaffold were able to synthesize their own ECM components, demonstrating the ability to restructure the scaffold during development (70). Lung cancer cells, when grown on a decellularized scaffold, displayed proliferation rates closer to what is seen *in vivo* than when compared to 2D culture conditions (72). Also, histological analysis of these cells displayed a representation of EMT *in vitro*. Colorectal carcinoma cells cocultured with fibroblasts resulted in enhanced invasion of the cancer cells into the scaffold, demonstrating an interaction similar to that seen between the tumor cells and stroma *in vivo* (68). Development of the cells also retained the time-efficient nature of *in vitro* models, with evidence of differentiation and invasion typically seen after 14 days (68).

This model system also allows for dynamic culturing conditions. Static conditions are not representative of those seen *in vivo*, and creating an *in vitro* system with dynamic flow conditions brings these models closer to bridging the gap. One method of supplying decellularized scaffolds with dynamic conditions is through the application of a bioreactor system that provides regulated flow of medium surrounding the scaffold and cells (73).

Overall, a model system implementing 3D cell culture on decellularized matrix scaffolds provides a very flexible and agile system, allowing for the interaction between multiple cell types in a biologically relevant environment while still retaining the efficiency seen *in vitro*.

1.4 Optical imaging modalities

As the development in model systems becomes more complex and detailed, so also must the methods in which the models are assessed and visualized. Optical imaging provides an opportunity for the real-time analysis of cell growth and development, to ensure the establishment of a useful endpoint for multiple cell lines. However, due to the depth and density of the decellularized matrix, traditional fluorescence microscopy is not sufficient to clearly image cells through such a dense scaffold.

1.4.1 Confocal Microscopy

Confocal laser scanning microscopy (CLSM) is a fluorescent imaging technique which may be used for the production of clear and focused images of cells in a scaffold system. In CLSM, light from a laser is focused on exciting a small portion of the sample. During emission, the light path is focused through a pinhole before reaching the detector, effectively removing any out-of-focus planes. This excitation may then be repeated at varying focal depths, resulting in a number of in-focus planes. These planes may then be stacked, creating a clear 3D image of the sample (74). When applied to imaging scaffolds of decellularized matrix, this technique allows for clear visualization at a greater depth than other optical imaging solutions. A similar technique, known as spinning disk confocal laser microscopy (SDCLM), works on the same principles of sample illumination as CLSM. However, through the application of a spinning disk with a series of pinholes, multiple points may be focused and imaged simultaneously (75)

1.4.2 Fluorescent reporter genes

Fluorescent reporter genes may be employed as a useful tool for imaging cells through SDCLM. However, for reporter genes to function properly, they must have been previously transduced into any cell lines used. Due to this necessity, fluorescent reporter genes are most useful for reliably and repeatedly imaging established cell lines.

Green Fluorescent Protein (GFP) is one such fluorescent reporter gene. GFP absorbs blue light and is excited at a wavelength of ~470nm, and emits green light at a wavelength of ~510nm (76). One consideration that should be made when imaging with GFP, however, is that there typically is some endogenous autofluorescence seen in tissues that may reduce the sensitivity or specificity of the image.

Tissue autofluoresence may be limited with the use of a fluorescent reporter in the near-infrared range, which has been shown to generate less autofluorescence when compared to emission at a lower wavelength (77). Nitroreductase (NTR) is a flavoprotein that is responsible for the reduction of nitro groups, and is currently used in pre-drug therapies due to its reduction capabilities (78, 79). However, the reduction potential of NTR may also be used as a fluorescent reporter gene in conjunction with CytoCy5s. CytoCy5s is a quenched, near-infrared probe that, when reduced by NTR, emits a fluorescent signal. Cytocy5s together with NTR is excited at a wavelength of ~631nm, and emits light a wavelength of ~688nm (80). With multiple potential reporter genes, it is also possible to image and distinguish more than one cell line simultaneously in a co-culture situation.

1.4.3 Imaging unlabeled cell lines

The most significant limitation seen in the use of fluorescent reporter genes is that the cells must be previously prepared for that precise purpose. However, with many analysis and characterization models relying on rapid availability of primary material, it is necessary to use an imaging solution that does not require any alteration or manipulation of the cells. Acetoxylmethyl Calcein (Calcein-AM) is an uncharged, lipophilic variant of Calcein that is able to freely and easily cross the cell membrane. Inside the cell, nonspecific esterases cleave the lipophilic blocking groups from Calcein-AM, resulting in a fluorescent form of Calcein that may

no longer freely leave the cell (81). When active, Calcein-AM has an excitation wavelength of ~488nm, and an emission wavelength of ~520nm. Unlike the previously mentioned fluorescent reporter genes, Calcein-AM will provide a signal for any viable cells present.

2 Aims

PDAC is a disease characterized by high mortality rates and low treatment efficacy, and late-stage detection caused by a delayed onset of symptoms further increases the need for novel and effective therapeutic strategies. Currently, focus is being shifted to the complex tumor microenvironment, which has been shown to both drive PDAC progression and impair treatment efficacy. Efficient and accurate preclinical models are therefore necessary to serve as a foundation for research driving therapeutic developments. With the goal of creating a system retaining the efficiency of *in vitro* models while also approaching the biological relevance typically reserved for *in vivo* models, we are striving towards an effective experimental platform for the application of novel therapeutics. In developing this model, our objectives are as follows:

- Design and optimize a system in which PDAC cells may be grown and followed in real time for the establishment of dynamic endpoints
- Apply and validate this system through the assessment of PDAC cells grown in monoculture
- Analyze interactions of PDAC and stromal cells within the system, moving closer towards a more representative system
- Comparison of results with other clinically relevant model systems

3 Materials and Methods

3.1 Cell Experiments

3.1.1 Cell Culture

All work involving cells was carried out under sterile conditions using a laminar flow bench with a HEPA filter. Cells were grown in 75 cm^2 tissue culture flasks (VWR International, ltd., Radnor, PA, USA), incubated at 37°C with a CO_2 concentration of 5%. Adequate cell growth and maintenance of sterility were ensured though daily observation under microscope.

All pancreatic cell lines were kindly provided by Anders Molven (Clinical Institute 1, University of Bergen). MIA PaCa-2 cell lines were cultured in a complete medium consisting of Dulbecco's Modified Eagle Medium (DMEM)-High Glucose, with 10% Fetal Bovine Serum (FBS), 2.5% Horse Serum (HS), 2% L-Glutamine (L-G) (Thermo Fisher Scientific, Waltham, MA, USA), and 1% Sodium pyruvate. MIA Paca-2 cells were split at a ratio of 1:10 into new complete medium twice per week, after reaching approximately 1 x 10^7 cells.

PANC-1 cell lines were cultured in a complete medium consisting of DMEM-High Glucose, with 10% FBS, 1% L-G, and 1% Sodium pyruvate. PANC-1 cells were split at a ratio of 1:4 into new complete medium twice per week, after reaching approximately 5 x 10^6 cells.

BxPC-3 cell lines were cultured in a complete medium consisting of Roswell Park Memorial Institute (RPMI)-1640 medium, with 10% FBS, 2% L-G, and 1% Sodium pyruvate. BxPC-3 cells were split at a ratio of 1:3 into new complete medium twice per week, after reaching approximately 4 x 10^6 cells.

BJ human fibroblasts were kindly provided by Donald Gullberg (Department of Biomedicine, University of Bergen). BJ fibroblast cell lines were cultured in a complete medium consisting of DMEM-High Glucose, with 10% FBS, 1% L-G, and 1% Penicillin/Streptomycin (P/S). BJ fibroblasts were split at a ratio of 1:3 into new complete medium twice per week, after reaching approximately 4 x 10^6 cells.

When passaging each cell line, medium was removed from the flask, and the cells were then washed with 10 mL phosphate-buffered saline (PBS). After removal of the PBS, 2 mL of Trypsin was added and the cells were incubated at 37°C for 5 minutes, or until completely detached. Trypsin was then inactivated through the addition of fresh complete medium, and the suspended cells were seeded at their appropriate ratio into a new 75 cm^2 flask before returning to the incubator.

3.1.2 Freezing of Cells

All cells were frozen in medium containing 95% complete medium and 5% Dimethyl sulfoxide (DMSO). Cells were first counted, and then pelleted at 1200 RPM for 5 minutes at room temperature. The pelleted cells were resuspended in their respective freezing medium, before transfer into 2 mL low-temp freezer vials (VWR International, ltd., Radnor, PA, USA), at a concentration of 1 x 10^6 to 2 x 10^6 cells per vial. The vials were incubated overnight at -80°C in either Mr. Frosty freezing containers (Thermo Fisher Scientific, Waltham, MA, USA) filled with isopropyl alcohol, or CoolCell freezing containers (BioCision, San Rafael, CA, USA) to ensure a cold rate of freezing of approximately 1C/minute. Once fully frozen, the vials were then transferred to cryoboxes stored at -80°C.

3.1.3 Thawing of Cells

Vials containing 1 x 10^6 to 2 x 10^6 cells were transferred from -80°C storage to a laminar flow bench, where they were thawed at room temperature until completely defrosted. 4 mL complete medium was added to the cells before transfer into a 15 mL Falcon tube (Sarstedt, Nümbrecht, Germany). The cells were then pelleted at 1200 RPM for 5 minutes at room temperature, and washed twice with complete medium before being transferred to a 75 cm^2 flask in 10 mL complete medium.

3.2 Viral transduction of BJ fibroblasts

3.2.1 Production of virus

4 x 10^6 293T cells (DSMZ - The German resource center for biological material) were seeded in 6 mL DMEM + 10% FBS medium on a 10 cm petri dish (Sarstedt, Nümbrecht, Germany) and incubated for 8 hours at 37°C. Once the cells were attached to the plate following incubation, 6

µL of chloroquine was added to the dish. Directly after chloroquine addition, a mixture was prepared of 195 µL 2M $CaCl_2$, 9 µg pPAX2 I viral vector (James Lorens, Department of Biomedicine, University of Bergen), 0.9 µg pMD2 II plasmid (James Lorens), 9 µg cd502 NTR (System Biosciences, Palo Alto, CA, USA), and 1295 µL filtered milliQ water. 15 minutes following the addition of chloroquine, 1527 µL Hepes buffered saline (HeBS) was added to the mixure, which was then air-bubbled for 20 seconds using an autopipette, and added dropwise to the dish.

The petri dish was then incubated for 16 hours at 37C, after which the medium was removed and replaced with 10 mL fresh DMEM + 10% FBS medium. The dish was incubated again for 8 hours, after which the medium was replaced with fresh DMEM + 30% FBS medium and transferred back to incubation for 24 hours.

3.2.2 Transduction of BJ fibroblasts

1 x 10^4 BJ fibroblasts were seeded in one well of a 24-well plate (Techno Plastic Products AG, Trasadingen, Switzerland) and incubated for 8 hours at 37°C to allow for cell attachment. The medium from the previously transfected 293T cells was then collected and transferred to a 15 mL Falcon tube. The tube was sealed with parafilm and centrifuged at 1250 RPM for 5 minutes to remove any remnant 293T cells. The resulting supernatant was then transferred to a fresh 15 mL Falcon tube. The medium in the well containing fibroblasts was then replaced with 2 mL of the collected supernatant (Estimated viral titre: 3 x 10^6 transducing units (TU)/mL), with the remaining volume stored in 1 mL aliquots at -80°C. The fibroblasts were incubated for 24 hours before the medium was replaced with 500 µL fresh complete medium.

3.2.3 Preparation of cells for flow cytometry

1 x 10^5 cells were incubated with complete medium in 6-well plates (Thermo Fisher Scientific, Waltham, MA, USA) for 24 hours at 37C, after which the medium was replaced with 2 mL fresh complete medium + 2 µL 1 mM CytoCy5s (Elvira García de Jalón Viñegra, Clinical Institute 2, University of Bergen) for a final concentration of 1 µM CytoCy5s. The cells were incubated in medium containing CytoCy5s for 1 hour, before washing with 2 mL PBS. 500 µL of trypsin was added to the cells, and they were then incubated for 5 minutes at 37°C. Trypsinization was halted

with the addition of 1.5 mL fresh complete medium, and the cells were transferred to a flow tube. The cells were then pelleted at 1200 RPM for 5 minutes and washed twice in PBS + 2% bovine serum albumin (BSA). After washing the cells were pelleted once again, and the supernatant was removed, leaving a small volume of PBS + 2% BSA in which the cells were resuspended for analysis using the BD Accuri C6 flow cytometer (BD Biosciences, San Jose, CA, USA). Viable, single cells were selected through gating in CFlow Plus (BD Biosciences, San Jose, CA, USA), and results were analyzed and processed using FlowJo V10 (BD Biosciences, San Jose, CA, USA). Live cells were first gated based on forward scatter (FSC) area and side scatter (SSC) area, followed by single cell selection based on the ratio of FSC area to FSC height.

3.2.4 Preparation of cells for sorting with FACS

Cells were expanded to approximately 90% confluence in a 75 cm^2 flask before preparation for cell sorting. The medium was removed from the flask, and replaced with 7 mL complete medium + 7 µL 1 mM CytoCy5s and incubated for 1 hour at 37°C. The medium containing CytoCy5s was then removed, and the cells were washed with 10 mL PBS. 2 mL of trypsin was then added to the cells, and they were then incubated for 5 minutes at 37°C. Trypsinization was halted with the addition of 8 mL fresh complete medium. The cells were then transferred to a 15 mL Falcon tube, and pelleted at 1200 RPM for 5 minutes. The cells were resuspended in 5 mL PBS + 2% BSA and filtered through a 40 µm strainer (VWR International, ltd., Radnor, PA, USA) into a 50 mL Falcon tube. The cells were pelleted once more at 1200 RPM for 5 minutes, and resuspended in a mixture containing 100 µL Hank's Balanced Salt Solution (HBSS) and 100 µL deoxyribonuclease (DNAse) I. The cells were then incubated in this mixture for 30 minutes at room temperature to prevent aggregation and clumping of cells. 1 mL PBS + 2% BSA was then added before transferring the cells to a 15 mL Falcon tube.

3.2.5 Confirmation and selection of NTR positive cells

The recently transduced BJ fibroblasts were analyzed for NTR positivity using fluorescence-activated cell sorting (FACS). The fluorescent potential for the fibroblasts was screened with FACS, and the 10% brightest cells were selected and passaged. The cells were sorted using FACS ARIA II (BD Biosciences, San Jose, CA, USA), and the 10% most positive cells selected were transferred to a 15 mL collection tube containing 5 mL complete medium + 1% P/S. Once

sorting was completed, the collection tube was centrifuged at 1200 RPM for 5 minutes, and the cells were resuspended in the appropriate volume of fresh complete medium + 1% P/S and seeded on the appropriate plate. Once the sorted cells were expanded to approximately 4 x 10^6, NTR positivity was re-evaluated with flow cytometry. Sorting and evaluation were then repeated until approximately 95% of the fibroblasts were positive for NTR signal.

3.3 SISser scaffold system preparation

3.3.1 Cell crown production

Cell crowns were produced with a Form 2 3D printer (Formlabs, Somerville, MA, USA), using High Temp resin (Formlabs, Somerville, MA, USA). After printing was complete, the crown structures were carefully removed from the build plate with a scalpel blade, and soaked in isopropyl alcohol for 15 minutes. The cell crowns were then dried using compressed air to remove any excess print material. The material was cured in a UV chamber in two rounds of 20 minutes.

3.3.2 WST-1 toxicity assay

2 mL MIA PaCa, BxPC-3, and PANC-1 complete media were incubated with samples of White, High Temp, or Dental SG material (Formlabs, Somerville, MA, USA), silicone, Polyether ether ketone (PEEK) material (Fraunhofer Institute, Würzburg, Germany), or no added material. One material sample was incubated per complete medium at 37℃ for 72 hours to generate conditional medium.

MIA PaCa-2, BxPC-3, and PANC-1 cells were split into numbers of 7 x 10^3, 10 x 10^3, and 10 x 10^3 cells respectively. The cells were pelleted at 1200 RPM for 5 minutes, and resuspended in 100 µL of each conditional medium in triplicate before transfer to a 96-well plate (Techno Plastic Products AG, Trasadingen, Switzerland). 100 µL of each experimental medium was also added to the 96-well plate without cells. The plate was then incubated at 37℃ for 72 hours.

After incubation, the medium was removed from each well, replaced with fresh complete medium + 10% cell proliferation assay reagent WST-1, and incubated once more for 5 hours. After incubation, the viability of cells in each well was analyzed using a Spectra Max Plus 384

microplate reader (Molecular Devices, San Jose, CA, USA) via absorbance (WST-1: 490 nm Background: 620 nm). The absorbance of wells containing no cells was averaged for each cell line, and this average was subtracted from each well containing cells to obtain the actual absorbance.

3.3.3 Production of SISser matrices

Porcine intestine was received as leftover material from surgical training subjects from the Laboratory Animal Facility, Department of Clinical Medicine, University of Bergen, and the lumen was flushed with tap water until no feces was visible. The intestine was then cut into sections approximately 10 cm in length, and each sample was flushed once again with tap water. Each section was then inverted with the use of long forceps, pulling the intestine through itself so that the mucosa surface of the lumen was facing outward. The mucosa surface, now on the exterior, was scraped off using forceps, resulting in sections with the submucosa facing outward and the serosa facing inwards. The sections were incubated in PBS + 1% P/S over night at 4C under agitation.

Each section was then washed three times with PBS, and filled with an 82 mM solution of sodium deoxycholate (DOC). Each section was clamped at both ends to seal the DOC solution inside. The sections were then incubated in DOC solution for 90 minutes at 4C under agitation to rid the samples of cellular material. After incubation, the sections were emptied of DOC solution and filled with PBS, re-securing both ends to prevent leakage, and washed in PBS for 60 minutes at 4C under agitation. The clamps were then removed, and each section emptied before washing in PBS + 1% P/S for 5 hours at 4C under agitation. PBS + 1% P/S was replaced every 60 minutes, and after the fifth change the sections were left overnight in fresh PBS + 1% P/S at 4C under agitation.

A DNase solution was prepared consisting of 50 mg DNase I (STEMCELL Technologies, Vancouver, Canada) + 300 ml warm PBS (+Ca/Mg) + 1% P/S. The SISser sections were incubated in the DNase solution for 2 hours at 37C under agitation to remove any remnant DNA material. After incubation, the sections were washed three times in PBS for 60 minutes at 4C under agitation, and were kept in fresh PBS + 1% P/S at 4C.

3.3.4 Mounting of decellularized matrix

SISser scaffolds used in mounting were obtained from the Translational Center for Regenerative Therapies, Fraunhofer Institute, Würzburg, Germany, received as 3 to 5 cm tubes of decellularized material, shipped at 4C in PBS. Scaffolds were processed as described (Section 3.3.3) and sterilized before shipment. Each scaffold was first spread and flattened with the use of forceps onto a 10 cm petri dish. The scaffolds were then cut along the side of the tube approximately 5 mm from the edge with a scalpel blade from one open end to the opposite. Using forceps, the scaffolds were opened from the recently cut side, and spread flat against the petri dish. The scaffolds were then divided into segments of approximately 1 to 2 cm^2, before spreading across the bottom surface of a cell crown. The outer ring of the crown system was then slid over the crown to secure the scaffolds, and each complete crown was added to one well of a 12-well plate (Thermo Fisher Scientific, Waltham, MA, USA) containing 1 mL complete medium. 500 µL of complete medium was added to the interior of each crown, followed by incubation for 24 hours at 37°C.

3.3.5 Cell seeding and culturing on scaffolds

Cells were first counted, and an appropriate concentration was pelleted at 1200 RPM for 5 minutes before resuspension in complete medium. The medium inside each crown was removed, and replaced with 500 µL fresh complete medium containing the desired number of cells. The crowns were then incubated for 72 hours at 37°C to allow the cells to attach to the scaffold.

When imaging was not necessary, the cells remained in the interior of the crown, which was incubated for the duration of the experiment at 37°C. The medium in each well was replaced with fresh complete medium twice per week to ensure appropriate growth conditions.

3.3.6 Preparing scaffold system for imaging

When imaging was necessary, the orientation of the scaffolds needed to be inverted (Fig 3.1). Each crown was transferred into a 10 cm petri dish, and the outer ring was removed carefully so that the scaffold remained attached to the crown. The crown with the attached scaffold was then

placed on top of a fresh crown, oriented so that the bottom surfaces of each crown were touching. The excess matrix on the side of the original crown was then folded down using forceps so that it becomes attached to the new crown. The original crown was then removed, leaving only the new crown with the scaffold oriented so the cells were located on the outer surface. The outer ring was then slid over the new crown to secure the scaffold, and each complete crown was transferred back to the 12-well plate containing 1 mL fresh complete medium, with the addition of 500 µL fresh complete medium to the inner well. The medium in each well was replaced with fresh complete medium twice per week to ensure appropriate growth conditions.

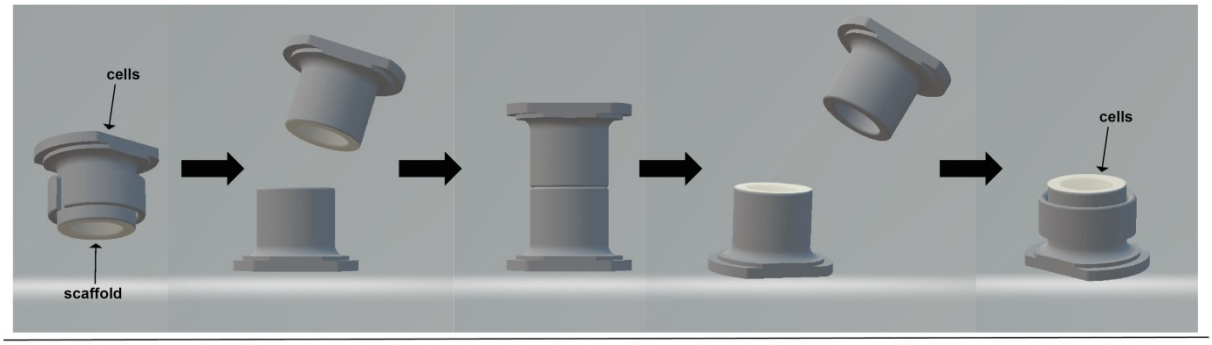

Figure 3.1 Flipping of scaffold orientation for imaging. Visualization of the method for flipping the scaffold orientation. By inverting the scaffold onto a second cell crown, cells may be oriented on the lower surface with minmal disturbance, in preparation for confocal imaging.

When preparing each crown for imaging, 1 mL fresh medium was first added to each well of a 6-well plate. Second, using forceps, each crown was transferred from a 12-well plate to 6-well plates so that the outer surface of the scaffold was in direct contact with the fresh medium and plate surface. Each crown was then imaged in this configuration.

The medium in the 12-well plates was replaced with fresh complete medium, and after imaging each crown was returned to the 12-well plates. The medium inside each crown was then replaced with 500 µL fresh complete medium and the plate was returned to incubation at 37°C.

3.3.7 Assessment of matrix permeability

Four replicates of SISser matrices were mounted onto crowns, and the inner well was filled with 10 µL Trypan Blue solution, 0.4% + 90 µL complete medium. The outer well was filled with complete medium containing no added dye. 10 µL samples were taken from both the inner and

outer wells at 0, 5, 10, 20, 40, and 60 minutes, as well as 2, 3, 6, 8, and 24 hours, and transferred to a 96-well plate. The concentration of Trypan Blue in each sample was measured with a NanoDrop 2000 spectrophotometer (Thermo Fisher Scientific, Waltham, MA, USA). Three measurements of 1 µL were taken from each sample, and absorbance (490 nm) was measured.

3.4 Confocal Microscopy

3.4.1 Image acquisition

All scaffolds were imaged using a Dragonfly 505 confocal spinning disk system (Andor Technologies, Inc, Belfast, Northern Ireland), and images were captured with the iXon 888 Life EMCCD camera within the confocal system. Image capture was directed and processed using FUSION imaging software (Andor Technologies, Inc, Belfast, Northern Ireland). Each image was taken at 10x magnification, utilizing a Z-stack depth of 150 to 300 µm with a 2 µm step size, depending on scaffold thickness. Due to the large surface area, three imaging fields were selected at random and captured in each scaffold to provide an overview of the entire sample area.

In every scaffold, the background matrix structure was imaged using a 561 nm laser line at 30% intensity, 100ms exposure time, and a 600 nm filter. No labelling dye was required to stimulate autofluorescence of the scaffold.

Scaffolds to be imaged with GFP were imaged using a 488 nm laser line at 5% intensity, 50ms exposure time, and a 525nm filter. No labelling dye was required to visualize GFP^+ cells.

Scaffolds to be labelled with CytoCy5s were imaged using a 637 nm laser line at 56% intensity, 50ms exposure time, and no filter. 500 µL complete medium containing 1 µM CytoCy5s was added to the inner well, while complete medium alone was added to the outer well. Scaffolds were then incubated for 1 hour in the culturing position before imaging. Fresh complete medium was added to both the inner and outer wells when transferring to the imaging position.

Scaffolds to be labelled with Calcein-AM were imaged using a 488 nm laser line at 5% intensity, 50ms exposure time, and a 525 nm filter. 500 µL complete medium containing 1 µM Calcein-AM was added to the inner well, and 1 mL complete medium with 1 µM Calcein-AM was added

to the outer well. The scaffolds were then incubated for 30 minutes in the culturing position before imaging. Fresh complete medium was added to both the inner and outer wells when transferring to the imaging position.

3.4.2 Image processing

All confocal images were processed using IMARIS 9 image analysis software (Oxford Instruments, Abington, UK). Fluorescent signal was quantified through the creation of surface volumes delineating areas of fluorescently labelled material. The overlap of multiple surface volumes was quantified with the use of the surface colocalization function, in which a new surface volume was generated from only voxels in which both surfaces were present.

3.5 Histology

3.5.1 Fixation and embedding of scaffolds

At the endpoint for each experiment where histological analysis was needed, the medium surrounding the crowns was removed, and each crown was washed with 1 mL PBS in the exterior well and 500 µL PBS in the interior. The PBS was then replaced with 4% paraformaldehyde (PFA) (VWR International, ltd., Radnor, PA, USA), and the crowns were incubated for 1 hour. After incubation, the PFA was removed and the crowns were washed again with PBS.

Each crown was then transferred to a 10 cm petri dish, and the outer ring was removed. Excess matrix attached to the side of the crown was flattened onto the petri dish using forceps, and cut away with a scalpel blade. The crown itself was lifted, leaving only the section of matrix containing cells on the dish. This matrix was then rolled using forceps and divided into three segments using a scalpel blade before transfer into histological cassettes for dehydration and paraffin processing.

Using a TP1020 tissue processor (Leica Biosystems, Wetzlar, Germany), the matrix scaffolds were run through a dehydration battery of two series of 80% ethanol, two series of 96% ethanol, four series of 100% ethanol, and two series of Xylene, submerged for 1 hour in each well. The

scaffolds were then transferred into two series of paraffin wax for 1 hour each to allow for paraffin infiltration.

After paraffin infiltration, the scaffolds were oriented vertically in metal molds containing paraffin wax, and placed on a cold plate until the paraffin was solid. The resulting paraffin blocks were removed from their molds and stored at 4°C overnight.

3.5.2 Slicing of histology samples

The paraffin blocks were transferred to storage at -20°C for 1 hour before slicing. Blocks were sliced using an RM2155 microtome (Leica Biosystems, Wetzlar, Germany). The blocks were trimmed in 45 µm slices until the cross section of the scaffold was visible on the surface of the block. The block was then sliced in 5 µm sections, and each slice was transferred to a water bath at 35°C. After any creases were removed in the water bath, the slices were then transferred flat onto microscope slides (VWR International, ltd., Radnor, PA, USA) and allowed to dry overnight.

3.5.3 Hematoxylin-Eosin (H&E) staining

Paraffin was removed from the slides through 2 changes of Xylene for 10 minutes each. The samples were then rehydrated in 2x 100% ethanol for 5 minutes, followed by 96% ethanol and 70% ethanol for 5 minutes each. The samples were washed briefly in distilled water, and stained in Harris hematoxylin solution (Merck, Kenilworth, NJ, USA) for 8 minutes. To remove excess hematoxylin, the samples were washed in running tap water for 5 minutes. After washing, the samples were transferred to 1% acid alcohol for 1 minute, followed by running tap water for 1 minute, and sodium bicarbonate for 1 minute. The samples were then washed in running tap water once more for 5 minutes, followed by 10 dips in 96% ethanol and counterstaining with Eosin working solution for 1 minute. The samples were then dehydrated in 96% ethanol, followed by two changes of 100% ethanol and two changes of Xylene for 5 minutes each. Finally, coverslips were mounted over the samples using a mounting solution of distyrene, tricresyl phosphate, and xylene (DPX). Samples were then left to dry overnight.

3.5.4 Masson-Goldner Trichrome staining

Paraffin was removed from the slides through 2 changes of Xylene for 10 minutes each. The samples were then rehydrated in 2x 100% ethanol for 5 minutes, followed by 96% ethanol and 70% ethanol for 5 minutes each. The samples were washed briefly in distilled water, and stained in Harris hematoxylin solution for 5 minutes. To remove excess hematoxylin, the samples were washed in running tap water for 5 minutes. Samples were then washed in 1% acetic acid for 30 seconds and stained in Azophloxine solution (Merck, Kenilworth, NJ, USA) for 10 minutes. The samples were washed again in 1% acetic acid for 30 seconds and stained in Tungstophosphoric acid orange G solution (Merck, Kenilworth, NJ, USA) for 1 minute. The samples were washed again in 1% acetic acid for 30 seconds and stained in Light green SF solution (Merck, Kenilworth, NJ, USA) for 2 minutes. The samples were washed again in 1% acetic acid for 30 seconds, followed by dehydration in 70% ethanol for 30 seconds, 96% ethanol for 30 seconds, two changes of 100% ethanol for 2 minutes each, and two changes in Xylene for 5 minutes each. Samples were mounted with DPX mounting solution and left to dry overnight.

3.5.5 Slide Imaging

Histology samples were imaged using a VS120 S6 slide scanner (Olympus Life Science, Waltham, MA, USA), collecting multiple imaging fields across the sample and stitching them together, resulting in a single image containing the entire sample field. Images were captured and stitched using VS-ASW S6 software (Olympus Life Science, Waltham, MA, USA). An overview of each slide was first imaged at 2x magnification, followed by the identification and imaging of sample fields at 10x magnification. The resulting images were processed using QuPath image analysis software (82).

3.6 Statistics

Statistical analysis of the difference in cell viability between each pancreatic cell line present in the WST-1 assay, as well as the difference in surface volumes of MIA PaCa-2, BxPC-3, PANC-1, and BJ Fibroblast cell lines was carried out using Student's t-test. For all statistical analysis, statistically significant results were determined by $p < 0.05$.

4 Results

4.1Optimization and validation of the 3D culture system

In collaboration with the Translational Center for Regenerative Therapies (Fraunhofer Institute, Würzburg, Germany) we were allowed access to samples of the original cell crown design, as well as the use of SISser decellularized matrix scaffolds. We wanted to establish a 3D model of PDAC utilizing the information and resources afforded to us, and to optimize and validate this system so that each application will produce accurate and reliable results.

4.1.1 Cell crown design

One feature of our system is the ability to follow cell growth in real time through confocal imaging, allowing dynamic endpoints to be set for cells with varying rates of growth. The original crowns were designed with the scaffold suspended and secured above the plate surface to allow for cell culturing with medium above and below the scaffold (Fig 4.1a). Confocal imaging requires the scaffold to be in contact with the imaging surface, so a new crown design was required to allow for both the culturing and imaging of cells on the scaffold. Various crowns were developed and tested (Fig 4.1b) before arriving at a design with both culturing and imaging orientations, and the ability to efficiently transfer between the two (Fig 4.1c).

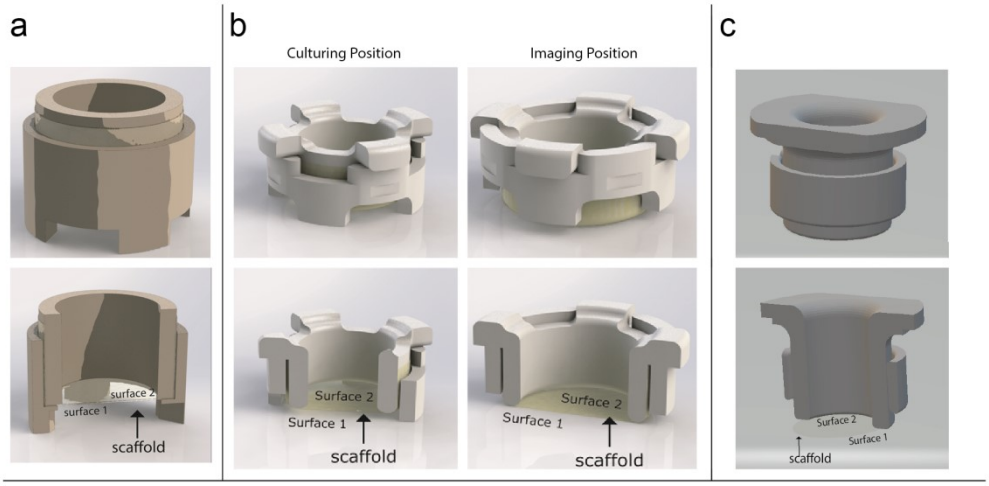

Figure 4.1 Models of cell crown designs. a.) Original cell crown design (Fraunhofer Institure, Würzburg, Germany). **b.)** Prototype cell crown design, allowing for transition between culturing and imaging positions. **c.)** Final cell crown design, the extended lip allows the cell crown to remain suspended in 12-well plates, while retaining surface contact in 6-well plates. All model renders provided by Spiros Kotopoulis, Department of Clinical Medicine, University of Bergen.

4.1.2 WST-1 Toxicity Assay

While the original crowns were developed using the biocompatible PEEK material, our newly designed crowns were produced via 3D printing with Formlabs White material, which has not been previously rated for biocompatibility. To ensure a lack of cytotoxic effects from the 3D-printed material, a WST-1 cell viability assay was carried out. MIA PaCa-2, BxPC-3, and PANC-1 cells were incubated in their respective complete media conditioned with PEEK, Formlabs White, Formlabs Dental SG, silicone, or no material. Cell viability was assessed by metabolic activity, which is directly correlated with absorbance (Fig 4.2a). MIA PaCa-2 cells, when cultured alongside silicone and Formlabs White, showed a significant decrease in metabolic activity compared to cells grown in medium with no material. When compared with Formlabs Dental SG, a material known to be biocompatible, this response was diminished, with a decrease in absorbance of approximately 8% compared with Formlabs Dental SG as opposed to the 18% decrease seen when compared with no material. A similar decrease in metabolic activity was also seen in PANC-1 cells cultured alongside PEEK and Formlabs White material, showing a decrease in absorbance of approximately 18% and 15% respectively. BxPC-3 cells, however, showed a significant increase in metabolic activity when cultured alongside Formlabs White material, and a trend of increased metabolic activity in all other materials with the exception of PEEK.

In practice, Formlabs White material was not durable enough to withstand the heat and pressure of autoclaving over time. Therefore, the material used to print crowns was changed to Formlabs High Temp. The viability assay was then repeated to analyze cells cultured alongside Formlabs High Temp and White materials. In this assay, there were no statistically significant differences in metabolic activity in any of the three cell lines (Fig 4.2b).

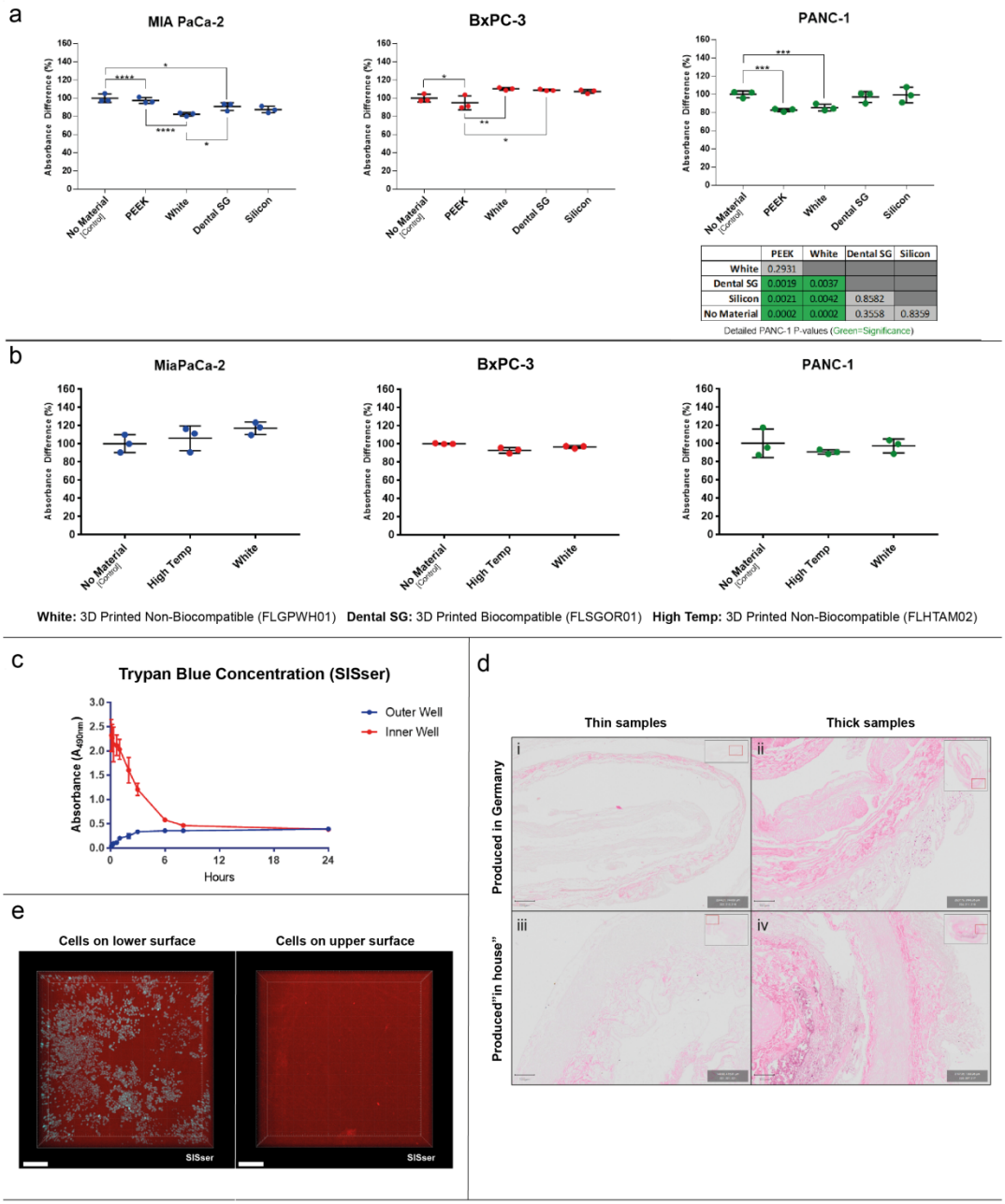

Figure 4.2 Validation and optimization of the model system a.) MIA PaCa-2, BXPC3, and PANC-1 cells were grown in conditional medium containing samples of various materials for 72 hours, after which cell viability was assessed through metabolic activity using a WST-1 assay. Absorbance (A_{450nm}-A_{620nm}) was normalized to the response of the "No Material" sample. A table of detailed significance values for PANC-1 cells was included to reduce clutter. **b.)** The viability assay was repeated to include the "High Temp" material. Error bars represent standard deviation. * = p<0.05, ** = p<0.01, *** = p<0.001, **** = p<0.0001 c.) Absorbance of medium in the inner and outer wells over 24 hours. 100 µL medium + Trypan Blue was added to the inner well, and 4 mL fresh complete medium was added to the surrounding well. Samples from both the inner and outer wells were analyzed using a spectrophotometer to determine Trypan Blue concentration over time. Error bars represent standard deviation. **d.)** Comparison of SISser matrices received from Fraunhofer Institute (i, ii) and SISser scaffolds produced by our lab (iii, iv). Both thin (i, iii) and thick (ii, iv) sections were analyzed. Scale bars represent 100 µm. **e.)** CytoCy5s signal from MIA PaCa-2 NTR+ cells seeded either on the upper or lower surface of the matrix. Red represents the background matrix structure (~633 nm), cyan represents a positive Cytocy5s signal from MIA PaCa-2 NTR+ cells (~691 nm). Scale bars represent 150 µm.

4.1.3 Assessment of scaffold permeability

The porousness of the scaffold in the crown system was analyzed to determine the ability of elements such as labelling dyes or therapy drugs to diffuse into and through the scaffold. Using SISser scaffolds, 100 µL complete medium + Trypan Blue was added to the inner well, with complete medium containing no dye in the surrounding well. Spectrophotometry was then used to detect absorbance corresponding with Trypan Blue (~490 nm) in both the inner and outer well over 24 hours, with absorbance directly correlated with Trypan Blue concentration (Fig 4.2c). After 6 to 8 hours, the concentration of Trypan blue is almost equal in both the inner and outer wells, with complete equilibrium by 24 hours.

4.1.4 "In-house" production of SISser

To streamline the use of our model system and increase self-sufficiency, production of the SISser scaffold was attempted in our lab. H&E-stained samples produced by our lab were compared with those received from the Translational Center for Regenerative Therapies (Fraunhofer Institute, Würzburg, Germany) in the absence of cells. While the decellularized matrices were generally uniform, sections from both origins showed occasional areas that appeared thicker, and samples from these areas were also compared. The normal, thin sections showed a similar pattern of H&E staining and similar structural patterns were present in both samples (Fig 4.2d i, iii). Scaffolds produced by our lab were noticeably thicker, averaging a thickness of approximately 300-500 µm, as opposed to a thickness of approximately 100-300 µm in the received samples. Areas from the visibly thicker sections showed structural similarities with the mucosa layer in both produced and received s (Fig 4.2d ii, iv). Samples from these sections produced in our lab displayed areas of hematoxylin staining, indicating the presence of cellular or DNA material.

4.1.5 Assessing imaging potential of the system

While confocal imaging provides a valuable tool for visualizing three dimensional samples with some degree of depth, SISser scaffolds are composed of dense materials that tend to diffract and block the penetration of light. The visualization of cells on both the upper and lower surfaces was tested by seeding MIA PaCa-2 NTR^{+} cells and imaging with CytoCy5s. Cells imaged on the bottom surface in direct contact with the imaging plate showed a clear and measurable signal,

while no fluorescence was able to be seen through the dense material of the SISser scaffolds (Fig 4.2e).

4.1.6 Optimization of Calcein-AM fluorescent dye

To allow for live-cell imaging of any cells seeded on the scaffold, Calcein-AM was selected as a candidate fluorescent dye that interacts with and labels all cells. To determine the optimal incubation strategy for the use of Calcein-AM, two methods of administration were tested. 1 μM Calcein-AM was added either to the inner well alone, or to both the inner and outer wells. Each condition was then monitored over time with confocal imaging (Fig 4.3a). When samples containing Calcein-AM only in the inner well were imaged, no signal could be seen from the cells at the 10 and 30 minute time points. The only discernible image from these images was the background autofluorescence from the scaffold. At the 60 and 120 minute time points, some sporadic signals appearing the size of a typical MIA PaCa-2 cell were visible, with the remaining areas becoming washed out.

Cells were easily discernible at each time point in the samples containing Calcein-AM in both the inner and outer wells. However, the most uniform and reliable signal appeared at 30 minutes. Images captured at 10 and 60 minutes show spots of weak or washed out signal where cells would be expected, along with patches of bright signal scattered across the image. This uneven staining seems to become more exacerbated after 120 minutes, and does not provide an optimal representation of the cells located on the scaffold.

4.1.5 Accuracy of Calcein-AM signal

To assess the accuracy of Calcein-AM staining, CytoCy5s was used as a known fluorescent marker for comparison. MIA PaCa-2 NTR^+ cells were incubated in 1 μM CytoCy5s for 1 hour and 1 μM Calcein-AM for 30 minutes, and the signals from each dye were visualized. The resulting images showed a similar pattern between the Calcein-AM and CytoCy5s reporter signals (Fig 4.3b).

To quantify the similarity between the Calcein-AM and CytoCy5s signals, surface colocalization was used. 50 x 10^3 MIA PaCa-2 NTR^+ cells were seeded on the submucosa and serosa surfaces

of the SISser scaffold. The surface volume of each channel was then analyzed using IMARIS image analysis software and the colocalization between the two surfaces was calculated. The colocalized surface volume, consisting of the voxels in which both the Calcein-AM and CytoCy5s surfaces intersect, represented 65% of the original Calcein-AM surface volume (Fig 4.3c).

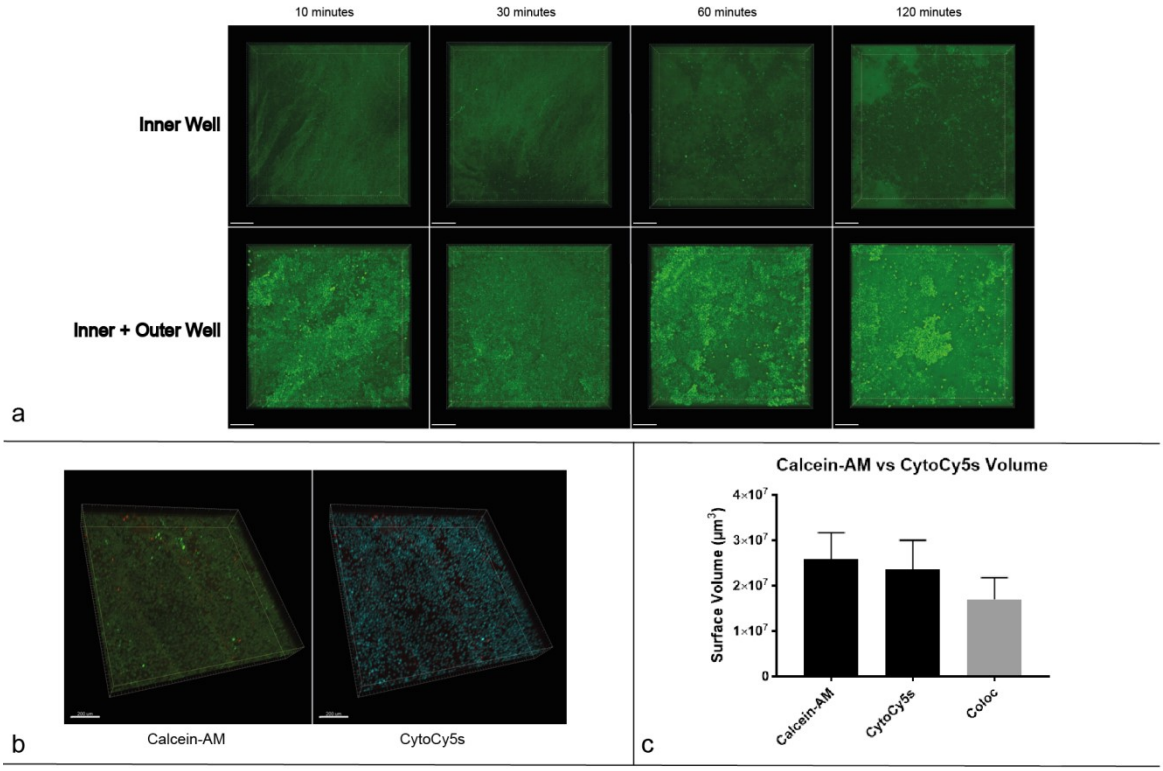

Figure 4.3 Assessment and optimization of Calcein-AM a.) Confocal images showing Calcein-AM signal. 12 x 10^3 MIA PaCa-2 cells were seeded on the submucose surface of the SISser scaffold, and cultured for 14 days. One sample was incubated with 1 μM Calcein-AM in only the inner well, while the other was incubated with 1 μM Calcein-AM in both the inner and outer well, imaging at 10, 30, 60, and 120 minutes for each sample. Images were captured in the green channel (~531 nm) at 10x magnification. **b.)** Direct comparison between Calcein-AM and CytoCy5s signal. 50 x 10^3 MIA PaCa-2 cells were seeded on the serosa surface of the SISser scaffold, incubated for 72 hours, and imaged. Before imaging, each sample was incubated for 1 hour with CytoCy5s (1 μM), and 30 minutes with Calcein-AM (1 μM). Calcein-AM was imaged using the green channel (~531 nm), CytoCy5s in the far-red channel (~690 nm), and the background matrix structure in the red chanel (~633 nm). **c.)** Colocalization of Calcein-AM and CytoCy5s signals, calculated using the surfaces function within IMARIS image analysis software. 50 x 10^3 MIA PaCa-2 cells were seeded on the mucosa, submucosa, and serosa surfaces of both the SIS-SER and SIS-MUC matrices and incubated for 72 hours before imaging. Error bars represent standard deviation. All scale bars represent 200 μm.

4.2 Pancreatic cell growth in monoculture

With a greater understanding of the behavior of the model system, it is important to determine how the system functions in combination with various pancreatic cancer cell lines. MIA PaCa-2, BxPC-3, and PANC-1 cell lines were selected to provide an overview of the response seen in cancer cells from different origins. Initially, GFP^+ cell lines were employed as a means of following their development in a reliable manner without the use of any fluorescent dyes.

4.2.1 MIA PaCa-2 monoculture

6×10^3, 12×10^3, 25×10^3, or 50×10^3 MIA PaCa-2 GFP^+ cells were seeded on the submucosa of SISser scaffolds, and growth was followed with confocal microscopy. After imaging was completed, the samples were fixed and prepared for histological analysis through H&E staining (Fig 4.4a). MIA PaCa-2 cells grew rapidly in comparison to the other two cell lines, reaching approximate confluency at day 14 in the lowest seeding number of 6×10^3. At other seeding concentrations, confluency was reached around day 10, with a clear pattern of increased cell concentration leading to a more rapid path to confluency. MIA PaCa-2 cells grew in a pattern of small colonies of circular cells expanding and combining until a mostly uniform surface was created over the scaffold.

Histological analysis shows areas of sporadic penetration of single or paired cells into the scaffold, along with instances of oval-shaped cell colonies appearing embedded within the scaffold. It is difficult to distinguish a pattern of invasion that aligns with an increased number of cells, as the most deeply embedded colony was seen in a sample initially seeded with 6×10^3 cells, with other examples of these colonies seen in samples seeded with 50×10^3 cells. However, as the concentration of seeded cells increases, so does the number of cells present on the surface of the scaffold, with the cells beginning to form loosely-packed layers in any initial number of seeded cells greater than 6×10^3.

4.2.2 BxPC-3 monoculture

The process of cell seeding, imaging, and histological analysis was repeated using similar numbers of BxPC-3 GFP^+ cells (Fig 4.4b). BxPC-3 cells were not able to grow with the ease seen in the MIA PaCa-2 samples, with a complete loss of cell signal by day 21 in the lowest

initial seeding number of 6 x 10^3. Only the highest seeding number of 50 x 10^3 was able to reach confluency, and did so around day 14. There was a pattern of increased initial seeding concentration leading to a larger area of cell coverage over time. The cells first developed into small, circular colonies which then expanded and combined to cover larger areas across the scaffold. However, the colonies of BxPC-3 cells were not comprised of spherical cells akin to the growth of MIA PaCa-2 cells, but grew in a more evenly-distributed and planar manner, with individual cells difficult to distinguish within the GFP signal.

Histological analysis showed; when cells were present, groups of evenly-distributed cells across the scaffold surface with areas of cells growing into the scaffold. As seen in a sample of 12 x 10^3 seeded cells, this growth into the scaffold does not require confluency to occur. Some cell colonies can also be seen growing within the scaffold, separated from those cells growing on the surface within samples seeded with 12 x 10^3 cells or greater. As the number of initially seeded cells increases, a greater area of the scaffold surface can be seen covered in BxPC-3 cells, with samples seeded with 50 x 10^3 cells showing almost complete confluency across the surface.

4.2.3 PANC-1 monoculture

The process of cell seeding, imaging, and histological analysis was repeated using PANC-1 GFP^+ cells (Fig 4.4c). PANC-1 cells did not grow as reticently as BxPC-3 cells; however they achieved a rate of confluency lower than in MIA PaCa-2 cells. Increasing from 6 x 10^3 to 12 x 10^3, confluency was reached around day 14, with cells almost reaching full confluency in the lower concentration by day 21. At these concentrations, the PANC-1 cells grew in populations of spherical cells expanding to distribute across the scaffold, with areas of denser cell concentration where individual cell distinction became difficult.

At seeded cell numbers of 25 x 10^3 and 50 x 10^3, dense colonies of cells were able to form before the cells could expand to cover the scaffold, resulting in a decreased surface coverage moving from 12 x 10^3 to 25 x 10^3 cells. This pattern was also seen in samples seeded with 50 x 10^3 cells, although the increased starting concentration appeared sufficient to drive more rapid growth. By the time of confluency in these seeding concentrations, a combination of dense colonies of cells

and individually distinguishable spherical cells can be seen, similar to that seen in the lower seeding concentrations.

Histological analysis showed cells growing across the scaffold surface, in a combination of tightly and loosely-packed cells. PANC-1 cells can also be seen growing into the scaffold directly from the surface, along with oval and circular shaped colonies of cells seen embedded more deeply within the scaffold. As seeding density is increased, a larger number of cells can be seen across the surface of the scaffold, and areas of growth into the scaffold seem to become more commonplace. Similarly to MIA PaCa-2 samples, more deeply embedded colonies can be seen across many seeding densities, including the lowest of 6×10^3.

4.2.4 Quantification of monoculture fluorescent signals

The growth of each cell line was quantified through analysis of the volume of surfaces created within IMARIS image analysis software, and surface volumes were plotted as a function over time (Fig 4.4d). Surface volume data showed that, in samples seeded with MIA PaCa-2 cells, the highest cell volume was achieved by day 10 in seeding densities of 25 and 50×10^3, or day 14 in seeding densities of 6 and 12×10^3. Samples seeded with BxPC-3 cells did not reach their maximum cell volume until day 21. PANC-1 samples reached a maximum volume at day 14 for seeding densities of 12 and 50×10^3, or day 21 in seeding densities of 6 and 25×10^3.

Samples containing MIA PaCa-2 and PANC-1 cells that reached a maximum volume before day 21 showed a continuous decline in surface volume until day 21. This response was not seen with BxPC-3 cells, as no samples reached a maximum volume prior to day 21.

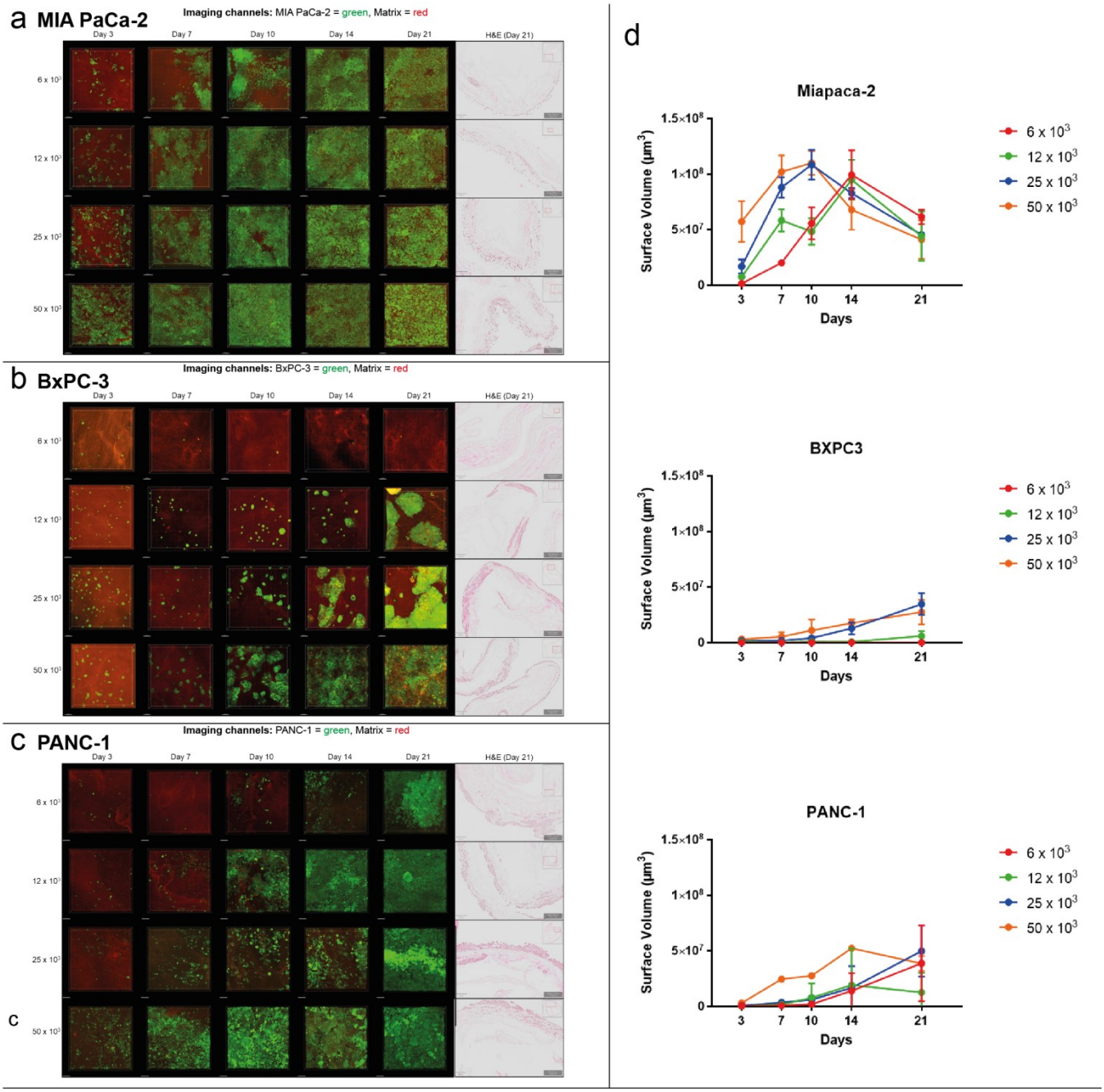

Figure 4.4 Confocal analysis of pancreatic cells grown in monoculture a.) Growth of MIA PaCa-2 GFP+ cells. 6 x 10^3, 12 x 10^3, 25 x 10^3, and 50 x 10^3, cells were seeded and imaged at 3, 7, 10, 14, and 21 days. Cells were imaged using the green channel (~531 nm), and background matrix structure was imaged using the red channel (~633 nm). All images were captured at 10x magnification. Scale bars represent 150 µm. Scaffolds were then fixed after 21 days, and histological analysis was carried out through H&E staining, imaged at 10x magnification and enlarged for detail. Scale bars represent 100 µm. **b.)** Growth of BXPC3 GFP+ cells, under similar conditions **c.)** Growth of PANC-1 GFP+ cells, under similar conditions **d.)** Demonstration of MIA PaCa-2, BXPC3, and PANC-1 cell growth over time. Surface volume was calculated using the surfaces function within IMARIS image analysis software. Error bars represent standard deviation.

4.3 Preparation for coculture experiments

To expand the model system in a way that the seeded pancreatic cells may grow in a more representative environment, BJ human fibroblasts were chosen to be seeded in coculture with the pancreatic cells. To distinguish between pancreatic cells and fibroblasts in confocal images, a dual color system was necessary. Therefore, one of the cell lines in the coculture required a fluorescent reported using a wavelength that does not overlap with the emission of GFP. CytoCy5s was selected as a reporter to image BJ fibroblasts in the far-red emission range, requiring transduction of the fibroblasts with NTR.

BJ human fibroblasts were transfected with NTR as described in the methods (Section 3.2). Following successful transfection, NTR^+ cells were selected using FACS, and after two rounds of sorting a population of BJ fibroblasts with approximately 94% NTR^+ cells was attained (Fig 4.5a). However, after analyzing the response of wild-type pancreatic cell lines to CytoCy5s administration, BxPC-3 wild-type cells showed an increased response when compared to other NTR^- cells. When compared with the recently finalized BJ fibroblast NTR^+ cell line, approximately 70% of the BxPC-3 NTR^- signal overlapped with the positive signal from the BJ fibroblast NTR^+ cell line, with <1% overlap with PANC-1 NTR^- cells (Fig 4.5b).

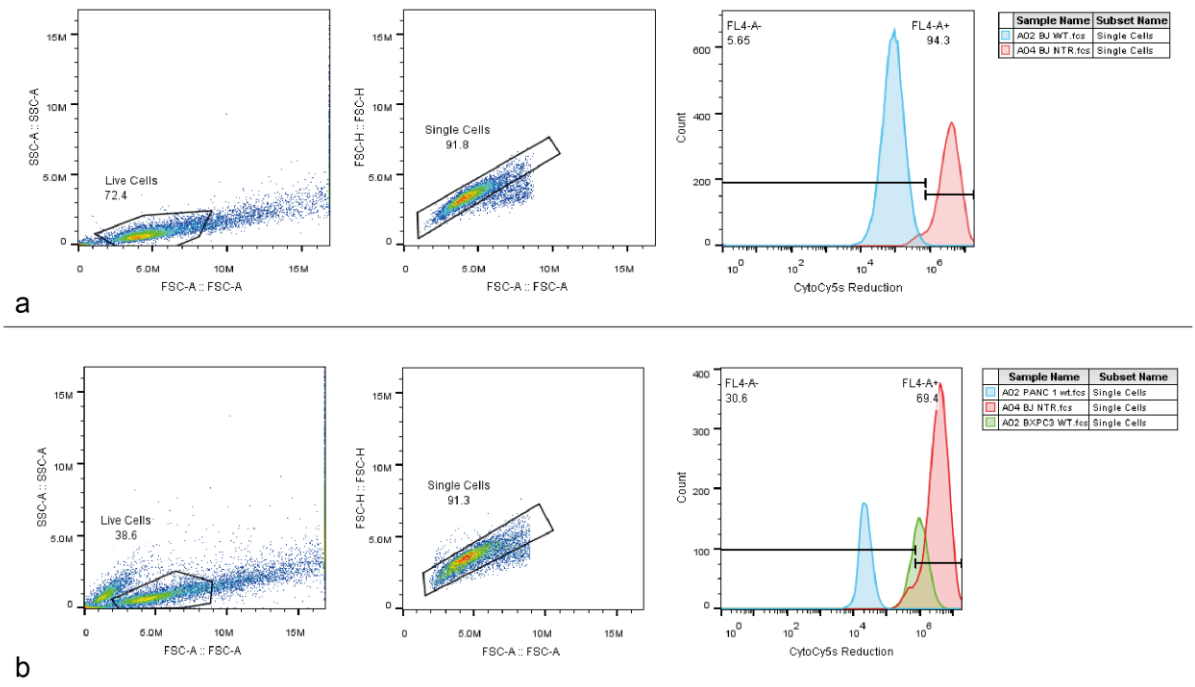

FIgure 4.5 Flow data indicating NTR positivity a.) CytoCy5s fluroescence intensity in BJ fibroblast NTR+ (Red) and NTR- (Blue) cells assessed by FACS after incubation with CytoCy5s (1 μM) for 1 hour, with an includedgating example. Histogram gating shows positivity of NTR+ (Red) cells. **b.)** CytoCy5s fluorescence intensity in BJ fibroblast NTR+ (Red), PANC-1 NTR- (Blue),and BxPC-3 NTR- (Green) cells assessed by FACS after incubation with CytoCy5s (1 μM) for 1 hour, with an included gating example. Histogram gating shows positivity of BxPC-3 NTR- (Green)cells.

4.4 Pancreatic cell growth in coculture with BJ fibroblasts

With a system in place to visualize and track multiple cell lines at once, GFP^+ BxPC-3, GFP^+ PANC-1, and MIA PaCa-2 wild-type cells were seeded on the submucosa of SISser scaffolds in coculture with NTR^+ BJ Fibroblasts to assess the effects of fibroblasts within the system. BxPC-3 and PANC-1 samples were followed with confocal imaging before histology, while MIA PaCa-2 samples were assessed only via histological analysis. This was to avoid cross-staining due to NTR^+ expression in the only available GFP^+ MIA PaCa-2 cell line.

4.4.3 MIA PaCa-2 + BJ Fibroblasts

12 x 10^3 MIA PaCa-2 cells were seeded on the submucosa surface of SISser scaffolds, either alone or in combination with 2.4 x 10^3 (20%) or 4.8 x 10^3 (40%) BJ Fibroblasts. 12 x 10^3 BJ fibroblasts were also seeded alone, and each condition fixed after 21 days for histology. Histological analysis of scaffolds containing MIA PaCa-2 cells showed a gradient of increasing

invasion potential correlated with increased fibroblast concentration (Fig 4.6d). When seeded alone, MIA PaCa-2 cells showed evidence of invasion into the scaffold, while typically remaining near or connected to cells on the surface. With the addition of 20% BJ fibroblasts, MIA PaCa-2 cells travelled farther from the surface, exhibiting the ability to move from one surface to the other by penetrating the entire scaffold. When BJ fibroblast concentration was increased to 40%, large colonies of MIA PaCa-2 were observable embedded deeply within the scaffold and independent of cells on the surface. BJ fibroblasts seeded alone were distributed sparsely across the surface and embedded within the scaffold.

4.4.2 BxPC-3 + BJ Fibroblasts

50 x 10^3 BxPC-3 cells were seeded on the submucosa surface of SISser scaffolds, either alone or in combination with 10 x 10^3 (20%) or 20 x 10^3 (40%) BJ Fibroblasts. 50 x 10^3 BJ fibroblasts were also seeded alone. When grown in coculture with BJ fibroblasts, BxPC-3 cells reached confluency more quickly than BxPC-3 cells grown alone (Fig 4.6a). When cultured without fibroblasts, BxPC-3 cells reached confluency at day 14, while confluency was reached at day 7 in both concentrations of added fibroblasts. Cells grew in a similar pattern to that seen in monoculture, grouped together in colonies of increasing size until confluency was reached.

Histological analysis of BxPC-3 samples show a general trend of decreased invasion as the number of added fibroblasts was increased. When seeded alone, invasion patterns appearing as cells extending away from the surface were present across much of the scaffold. With the addition of 20% BJ fibroblasts, combinations of invasion patterns were present. In some areas cells were growing from the surface into the scaffold, while small oval-shaped colonies were located within the scaffold. However, the instances of invasion were not as ubiquitous when compared to BxPC-3 cells seeded alone, with many areas showing no signs of invasion. With the addition of 40% BJ fibroblasts, very few instances of invasion were visible. The primary pattern of invasion when present was oval-shaped colonies of BxPC-3 cells embedded within the scaffold.

4.4.3 PANC-1 + BJ Fibroblasts

50 x 10^3 PANC-1 cells were seeded on the submucosa surface of SISser scaffolds, either alone or in combination with 10 x 10^3 (20%) or 20 x 10^3 (40%) BJ Fibroblasts. 50 x 10^3 BJ fibroblasts were also seeded alone. When grown in coculture with BJ fibroblasts, PANC-1 cells were able to grow more rapidly, with higher concentrations of cells visible at days 3 and 7 when fibroblasts were present (Fig 4.6b). PANC-1 cells grew in a similar pattern to that seen in monoculture under all conditions, with a combination of spherical cell clusters and dense cell colonies developing and spreading until confluency was reached. However, when cultured with 40% BJ fibroblasts, bright areas indicating tightly clustered cells were no longer present at day 21, instead appearing as a rather uniform distribution of signal intensity.

Histological analysis shows a trend of increasing invasion potential correlated with increased fibroblast concentration. When seeded alone, PANC-1 cells showed areas of single cells and oval-shaped clusters of cells embedded within the scaffold. The occurrence of these patterns was increased with the addition of 20% BJ fibroblasts, as well as the ability for cells to more commonly travel deeper into the scaffold. When cultured with 40% BJ fibroblasts, invasion was even more common, with a majority of the scaffold cross-section filled with cells in many areas.

4.4.4 Quantification of culture fluorescent signals

The growth of each cell line was quantified through analysis of the volume of surfaces created within IMARIS image analysis software, and surface volumes were plotted as a function over time (Fig 4.6c). Surface volume showed that BxPC-3 samples reached a maximum volume at day 7 when cultured with fibroblasts, and day 14 when cultured alone. Also, the surface volume of BxPC-3 cells in coculture with 40% BJ fibroblasts was significantly higher ($p<0.01$) than BxPC-3 cells seeded alone. PANC-1 samples reached a maximum volume by day 14 when cultured alone and with 20% fibroblasts. Surface volume of PANC-1 cells cultured with 20% BJ fibroblasts was also significantly greater ($p<0.05$) than when grown alone However, PANC-1 cells cultured with 40% BJ fibroblasts never reached this maximum volume, comprising a lower surface volume than the other two conditions after day 7.

Both BxPC-3 and PANC-1 showed a decrease in surface volume following the time point at which the maximum volume was reached. PANC-1 cells cultured with 40% BJ fibroblasts, despite never reaching the maximum volume, also demonstrated a decreased signal volume at day 21.

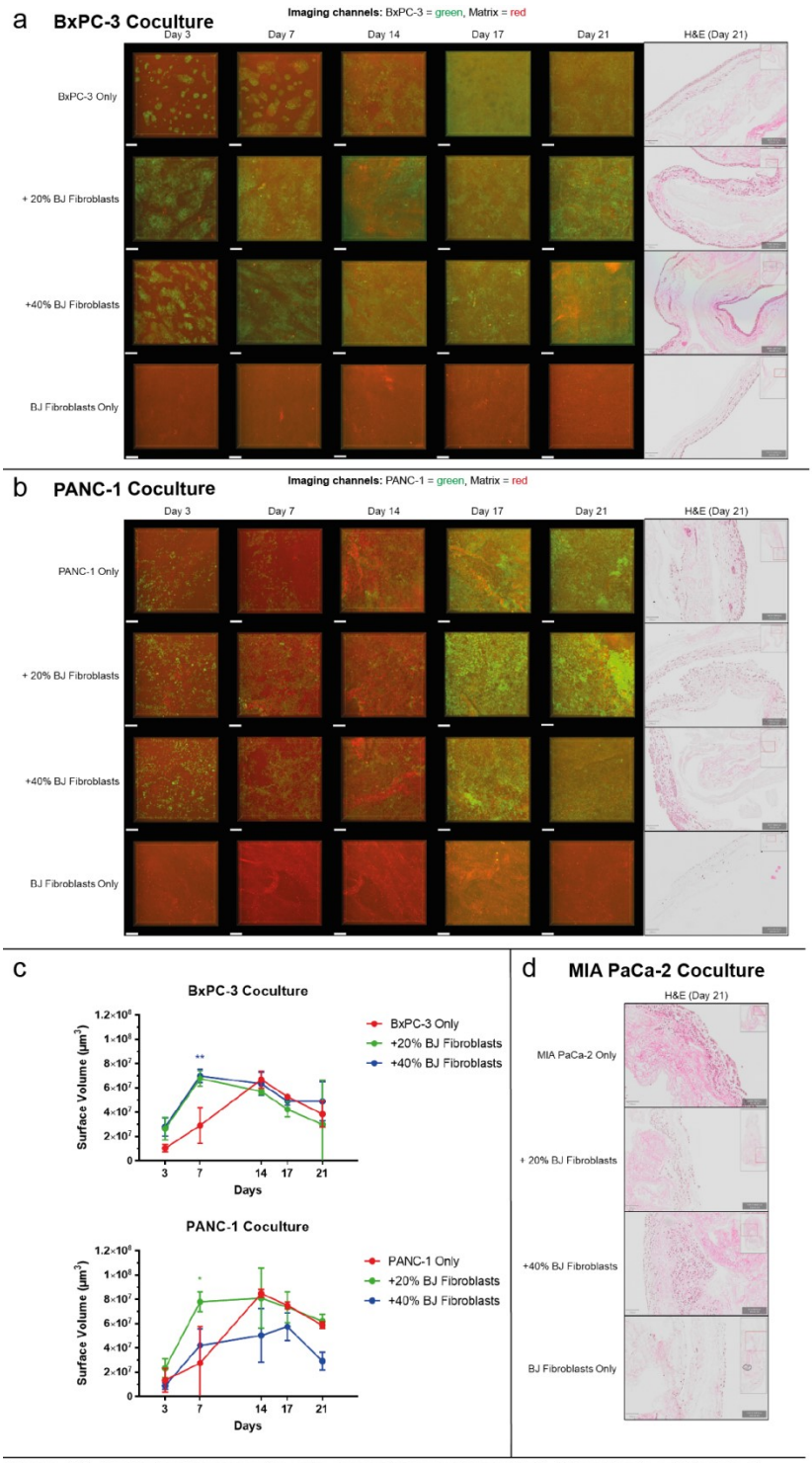

Figure 4.6 Analysis of pancreatic cells grown in coculture with BJ fibroblasts a.) Growth of BxPC-3 GFP+ cells, seeded at 50 x 10^3 cells alone or in combination with 10 x 10^3 (20%) or 20 x 10^3 (40%) BJ fibroblasts. 50 x 10^3 BJ fibroblasts were also seeded alone, and each condition imaged at 3, 7, 14, and 21 days. Cells were imaged in the green channel (~531 nm), and background matrix structure was imaged in the red channel (~633 nm). All images were captured at 10x magnification. Samples were fixed after 21 days, and histological analysis carried out via H&E staining, imaged at 10x magnification and enlarged for detail. **b.)** Growth of PANC-1 GFP+ cells under similar culturing and imaging conditions. **c.)** Quantification of BxPC-3 and PANC-1 cell growth over time. Surface volume was calculated using the surfaces function within IMARIS image analysis software. Error bars represent standard deviation. $p<0.05$ = *, $p<0.01$ = **. **d.)** Histological analysis of MIA PaCa-2 seeded at 12 x 10^3 cells alone or in combination with 2.4 x 10^3 (20%) or 4.8 x 10^3 (40%) BJ fibroblasts. 12 x 10^3 BJ fibroblasts were also seeded alone.

4.4.5 BJ Fibroblasts in coculture

Utilizing the two-color system, BJ fibroblast development was followed over time alongside PANC-1 cells (Fig 4.7a). Between day 3 and day 7, there was a decrease in signal intensity. This is quickly reversed by day 14 however, with the fibroblasts covering a much larger area. Following day 14, there is once again attenuation in signal at all concentrations, resulting in an inability to visually identify fibroblasts when PANC-1 cells were also present.

Quantification of surface volume (Fig 4.7b) demonstrates a similar pattern of development in all BJ fibroblast concentrations, achieving a peak volume on day 14. The pattern is also consistent with that seen in PANC-1 cells, where there is a drop in surface volume after reaching a maximum value.

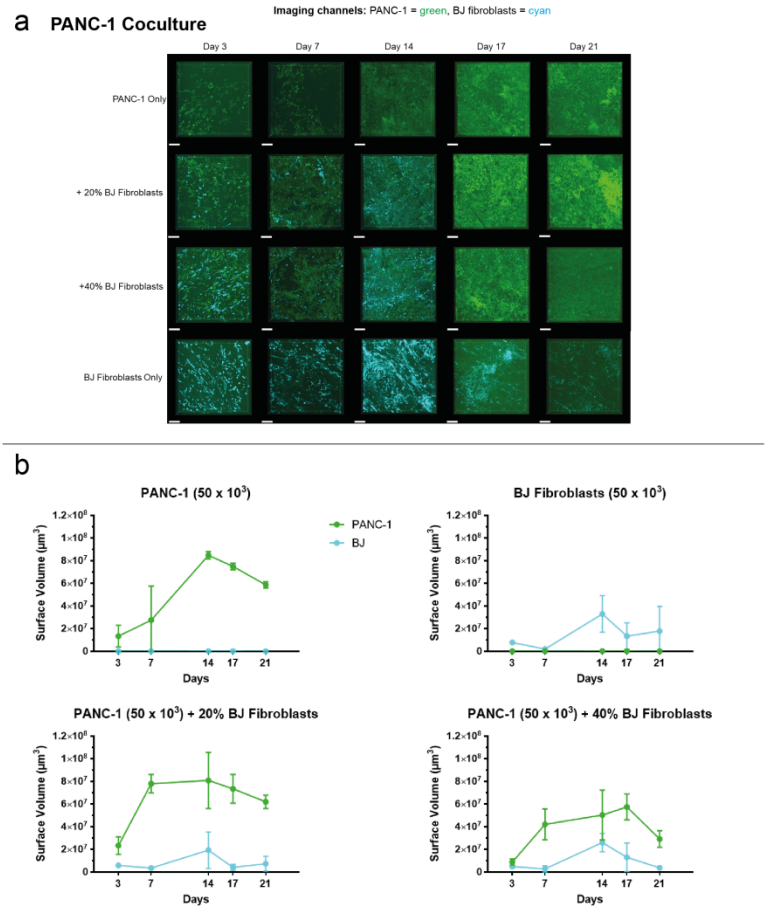

Figure 4.7 Comparison of PANC-1 and BJ fibroblasts in coculture a.) Growth of PANC-1 GFP+ and NTR+ BJ fibroblasts. 50 x 10^3 PANC-1 cells were cultured alone or in combination with 10 x 10^3 (20%) or 20 x 10^3 (40%) BJ fibroblasts. 50 x 10^3 BJ fibroblasts were also cultured alone, and each condition was imaged at 3, 7, 14, 17, and 21 days. PANC-1 cells were imaged in the green channel (~531 nm), and BJ fibroblasts were imaged in the far red channel (~691 nm, visualized as cyan). All images were captured at 10x magnification. **b.)** Comparison of PANC-1 and BJ fibroblast growth over time. Surface volume was calculated using the surfaces function within IMARIS image analysis software. Error bars represent standard deviation.

4.5 Comparison with established model systems

By comparing our system to standard *in vivo* models, a better understanding of its clinical relevance may be ascertained. Using Masson-Goldner trichrome staining, the cells and ECM may be more easily differentiated, allowing for a more accurate assessment of both (Fig 4.8). In collaboration with Anders Molven (Department of Clinical Medicine, University of Bergen) and Dag Hoem (Department of Gastrointestinal Surgery, Haukeland University Hospital), PDAC samples were collected from patients that underwent surgical resection after their informed consent. Processing and engraftment of samples was carried out by Gorka Ruiz de Garibay (Department of Clinical Science, University of Bergen), who provided the primary, orthotopic, and subcutaneous samples for staining.

When comparing the histological analysis of a primary tumor and subsequent orthotopic tumor in two PDX models, large areas of highly desmoplastic ECM are present in the primary material, while orthotopic tumors of the same origin lack these areas of desmoplasia (Fig 4.8b). A tumor arising from subcutaneous injection of MIA PaCa-2 cells shows even less evidence of desmoplasia, with the landscape consisting almost entirely of cellular material (Fig 4.8c). In contrast to the *in vivo* tumor models, our system demonstrates areas of cells embedded within the ECM more similar to the morphology seen in primary material (Fig 4.8a).

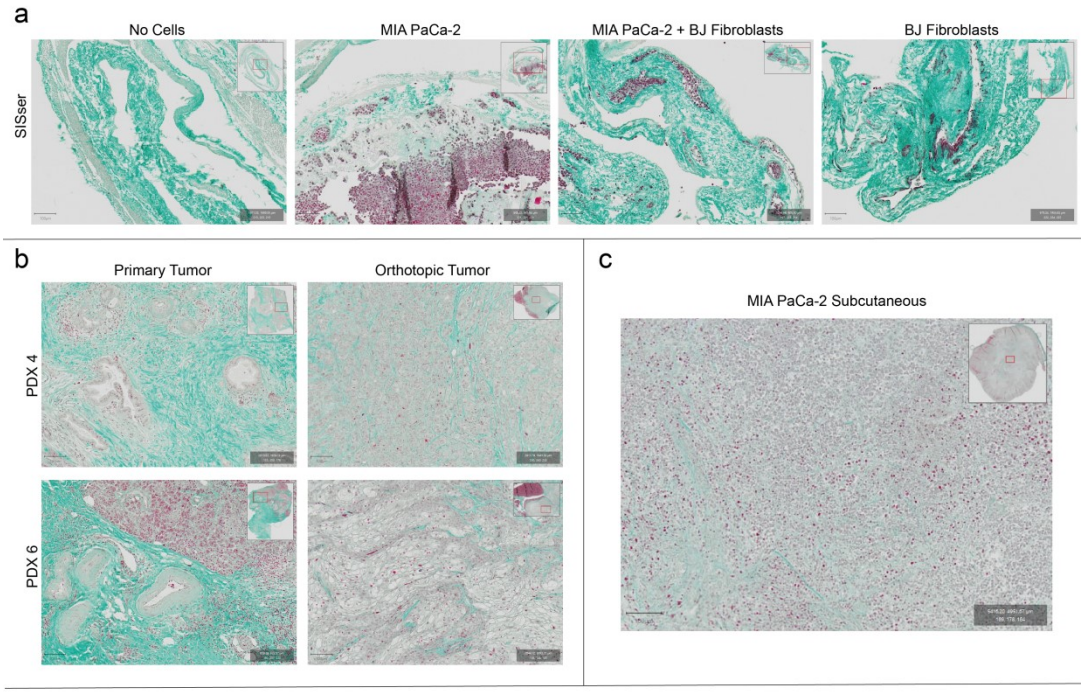

Figure 4.8 Comparison of SISser scaffolds with established preclinical model systems a.) Trichrome staining of SISser scaffolds containing various combinations of MIA PaCa-2 and BJ fibroblasts, highlighting the distribution of cells (Purple) and ECM (Green) **b.)** Sections from primary and orthotopic material from two PDX models. **c.)** Section from a tumor arising from the subcutaneous injectionof MIA PaCa-2 cells.

5 Discussion

PDAC is a disease plagued by difficult diagnose and ineffective treatment opportunities. Multiple factors lead to these issues, including the onset of symptoms at a late stage of disease progression and the complex tumor microenvironment that serves as a barrier to successful therapeutic strategies. This microenvironment consists of a complex system of multicellular interaction, with the effects of stromal cells, immune cells, and endothelial cells all coalescing around the PDAC tumor cells. Effective preclinical models are therefore necessary to allow for the characterization of the tumor-stroma interactions, which may provide some insights for potential therapeutic targets. Additionally, effective testing of novel therapeutics relies on accurate and reliable model systems, further increasing the need for potent preclinical models. With the preliminary design and development of a novel 3D PDAC model system, we hope to address these needs.

5.1 Optimization and validation of the 3D culture system

In the development our model system, one key aspect is the ability to follow cell growth in real time with the use of confocal microscopy. The original crowns we received are not compatible with this method of imaging due to a fixed scaffold position above the imaging plane, so a new design was necessary. Proper culturing conditions require the scaffold to be suspended to keep the system isolated and surrounded with medium, while confocal imaging requires the scaffold to be in contact with the plate surface. Multiple designs were drawn up and tested in an attempt to accommodate both positions, focusing initially on systems with two configurations that could be altered with physical manipulation (Results Fig 1b). This manipulation was a source of difficulty, leading to torn or dislodged scaffolds, contamination from extensive interaction, and inefficient use of time when imaging in larger batches. To negate these issues, a final design was implemented as a simple system meant to secure the scaffolds, with both imaging and culturing orientations possible depending on well size (Results Fig 1c). Removing the requirement of physical manipulation resulted in the reduction of damaged samples, occurrences of contamination, and time required for transitioning between imaging and culturing.

Production of the new crown design was carried out via 3D printing, using materials not previously rated for biocompatibility. When assessing the biocompatibility of printed material,

some effects on cell viability could be seen depending on the material cells were cultured alongside. However, while some of these differences may have been statistically significant, effects were not consistent across all materials or cell lines, and the combinations of materials and cell lines that did show evidence of toxicity only demonstrated a minor reduction in cell viability. Similarly, PEEK has been shown to display no cytotoxic or mutagenic activity (83), so the significantly lower absorbance seen in PANC-1 cells may be within an acceptable range for biocompatibility. The unique response of increased viability in BxPC-3 cells may be due to the genotypic expression separating these cells from MIA PaCa-2 and PANC-1, with only the BxPC-3 cell line containing a wild-type form of KRAS oncogene between the three cell lines (84).

After securing the details of the crown system supporting the scaffold, imaging potential was tested. Cells are typically seeded in the inner well, so that they come to rest on the upper surface of the scaffold. However, even when in contact with the imaging plate, no fluorescent signal was seen from cells on the upper surface of the SISser scaffold. This is most likely due a scattering and diffusion of the fluorescent signal as it travels through the dense scaffold. CytoCy5s was implemented as the reporter dye, with an emission wavelength of ~690 nm. As emission wavelength of a dye increases, so also does the ability to penetrate deeper tissue (85). Based on this, it can be assumed that dyes with shorter wavelengths, such as GFP and Calcein-AM, will similarly not be seen through the scaffold. Due to the inability of cell visualization on the upper surface of the scaffold, successful imaging requires the scaffold itself to be flipped to position the cells on the lower surface. Using this method, cells may be cultured in normal conditions on the upper scaffold surface until attachment, and then flipped for imaging and future culturing on the lower surface.

SISser scaffolds produced in our lab displayed similar morphology and structure to those received from the Fraunhofer Institute. The difference in overall size seen in our slides may be a result of varying anatomy between pigs. However, some samples produced in our lab showed areas of increased H&E staining when compared to our received samples. Due to a lack of access to adequate sterilization techniques, our samples did not undergo the same sterilization techniques as the samples received from the Fraunhofer Institute. Due to this, it is possible that the stained material represents the presence of bacteria or fungal activity, and proper sterilization

techniques would result in the removal of stained material. Additionally, the presence of staining could be a result of incomplete decellularization and removal of DNA material. In either event, if the scaffolds we produce are to be used in cell culture they will require proper sterilization.

5.2 Pancreatic cell growth in monoculture

When MIA PaCa-2, BxPC-3, and PANC-1 pancreatic cell lines were grown on the SISser scaffold in monoculture, each cell line showed a distinct pattern of growth. These growth patterns demonstrate that the model system is flexible enough to allow for the individualized growth of any seeded cells, and that cells do not simply conform to a pattern of growth directed by the scaffold interaction. Our ability to successfully follow these growth patterns also demonstrates the potential to assess the development and state of cells grown on the model system without the need for halting the experiment for fixation.

Samples that were able to successfully reach confluency prior to day 21 were all followed by a decrease in surface volume, possibly caused by cell cycle arrest leading to a decreased expression of GFP, or the detachment of cells during manipulation of the crown system for imaging.

One limitation of the information gathered from these confocal images is that they primarily demonstrate the location and growth of cells along the surface of the scaffold. As seen in the issue of imaging cells on the upper surface of the scaffold, signal interference is increased with the depth of cells within the scaffold structure. While the imaging platform is certainly able to provide images with some depth (Each image was captured with a thickness between 150 and 300 μm), it is quite difficult to distinguish visually between cells located on the surface of the scaffold and those that may have become embedded. However, the purpose of following cells with confocal imaging is not to accurately quantify growth over time, but rather provide some system through which standardized endpoints may be implemented across cell lines with unknown rates of growth.

Histological analysis demonstrated that a more detailed and accurate visualization of cell growth on the scaffold is possible once the endpoint is reached. The appearance of each cell line in this

histological analysis coincides with their respective confocal images across the surface. When assessing invasion potential, each cell line demonstrated some degree of embedding under all seeding conditions. BxPC-3 samples also show that confluence is not necessary for invasion of the scaffold. At 12 x 10^3 seeded cells, two separate areas of cell growth can be seen, with both displaying some amount of invasion into the scaffold. BxPC-3 samples at large also seem to show a greater ratio of embedded cells to surface cells when compared with MIA PaCa-2 and PANC-1 samples. This coincides with literature detailing the difference between these pancreatic cell lines, as BxPC-3 cells display a higher invasive potential in substrates such as fibronectin and laminin (86).

5.3 Preparation for coculture experiments

After confirmation of the ability to follow and assess pancreatic cells in monoculture, a more complex use of the model was applied, requiring a two-color system where two cell lines could be independently labelled and followed. After successful transduction and sorting, NTR^+ BJ fibroblasts were developed to produce a fluorescent signal with almost no overlap compared to NTR^- BJ fibroblasts or PANC-1 wild-type cells when incubated with CytoCy5s. However, the overlap seen in BxPC-3 wild-type cells with NTR^+ BJ fibroblasts indicates a similar fluorescent response between the two cell lines. One explanation for the increased fluorescence in BxPC-3 cells could be due to increased hypoxia. NTR^+ cells have an enhanced ability in the reduction of nitrile groups, leading the fluorescent emission in the presence of CytoCy5s (80). However, native nitroreductase activity may be increased under hypoxic conditions (87), indicating that a fluorescent signal in the presence of CytoCy5s may indicate hypoxia in NTR^- cell lines, such as wild-type BxPC-3. It is possible that the signal from these cells is due to the expression pattern of the cell line, as BxPC-3 cells are the only instance of pancreatic cells with wild-type KRAS expression out of the cell lines we used. However, the ability of CytoCy5s to label hypoxic conditions may have some benefit in testing other cell lines or growth conditions for hypoxia.

Based on the results of SISser membrane permeability (Fig 4.2c), more efficient usage of CytoCy5s was attained by administering only in the inner well and allowing the dye to enter and pass through the scaffold. While the permeability seen in Trypan Blue may not predict an exact

equilibrium curve for other dyes such as CytoCy5s, it does demonstrate a porousness of the scaffold and indicates the ability for the transfer of materials from the inner to outer well.

5.4 Pancreatic cell growth in coculture with BJ fibroblasts

With a system in place to image follow both pancreatic cells and fibroblasts independently; the two cells types were cultured both alone and alongside each other to assess any effects of interaction. Imaging analysis showed an overall increase in growth rate of both BxPC-3 and PANC-1 cells when cultured alongside BJ fibroblasts, indicating some form of interaction. An increased rate of proliferation due to interaction with fibroblasts correlates with patterns seen in PDAC, where growth factors and ECM components excreted by PSCs induces increased proliferation of tumor cells (24).

After reaching confluency, all conditions of both BxPC-3 and PANC-1 cells resulted in a decreased surface volume until the endpoint was reached. However, PANC-1 cells cultured with 40% BJ fibroblasts reached a maximum surface volume much lower than that shared between both PANC-1 cells seeded alone and with 20% BJ fibroblasts. One possibility for this subdued signal is that the increased concentration of fibroblasts drives the cells to invade the scaffold, as seen in experiments with colorectal cells on SISser scaffolds (68). As the cells move deeper into the scaffold structure, the fluorescent signal becomes more occluded due to the dense material surrounding the cells. This, coupled with a decreased number of cells on the surface, would result in a lesser amount of cells visualized and included in the surface volume quantification.

Histological analysis of BxPC-3, PANC-1, and MIA PaCa-2 cells in coculture with BJ fibroblasts also showed trends of pancreatic cell invasion potential driven by the presence of fibroblasts. PANC-1 and MIA PaCa-2 cell lines both showed a positive correlation between concentration of fibroblasts and magnitude of invasion, similar to previous experiments using colorectal cells (68). BxPC-3 cells, however, demonstrated a negative correlation, with much fewer areas of invasion seen as the concentration of fibroblasts was increased. This is unexpected in the context of the response seen in MIA PaCa-2 and PANC-1 cells, although the unique genetic composition of BxPC-3 cells may be responsible. It is possible that wild-type KRAS

expression present only in BxPC-3 cells is responsible for the vastly different responses compared to MIA PaCa-2 or PANC-1 cells that contain mutated KRAS expression.

5.5 Comparison with established model systems

With a greater understanding of the SISser model obtained from our experiments, it is important to compare this model with other standard systems to better understand where pancreatic cell lines grown on SISser scaffolds can fit in the landscape of preclinical analysis.

The lower concentration of ECM material present in both orthotopic and subcutaneous injection models demonstrates a tumor microenvironment dissimilar to the desmoplastic nature of primary tumors. This may potentially lead to a subdued role of the tumor stroma in these models, characterized by both a lack of ECM factors that drive tumor-stroma interaction and mechanical isolation of tumor cells within the desmoplastic core.

MIA PaCa-2 cells and BJ fibroblasts seeded on SISser scaffolds show an ECM density and morphology similar to examples of ECM in primary tumors. It is important to note however, that the MIA PaCa-2 cells were added to a pre-existing collection of ECM materials, and the ability of these cells to drive the secretion and development of their own ECM factors has not yet been determined. Masson-Goldner trichrome staining used to distinguish the ECM also colors all ECM factors with the same green hue, so it is possible that there are some compositional differences between the ECM in primary material and SISser scaffolds. Overall these comparisons are quite preliminary, though they provide insight on the potential for future directions in developing a representative model of PDAC.

One method in which the SISser model can be further analyzed is through the addition of primary PDAC material as opposed to genetically labelled pancreatic cell lines. Cell suspensions derived from primary tumors may contain multiple cell types biologically relevant to PDAC development, and it would be useful to assess their interaction and development in a SISser model. Before this can be accomplished, however, a method of labelling and following these cells will be necessary. Calcein-AM demonstrated the ability to fluorescently label unmodified cell lines, and would be useful for applications with primary material (Results Fig 3). When

compared with CytoCy5s, Calcein-AM signal covered a larger volume. One possibility for this is that Calcein-AM is present in a larger portion of the cytoplasm, whereas CytoCy5s signal appears more compact within the cell. Overall though, the volume of the colocalized surface was not significantly smaller than the Calcein-AM volume alone, indicating a statistical similarity between the two dyes.

Based on our results, Calcein-AM does not possess the same ability as CytoCy5s to perfuse through the scaffold in a way that it can still label cells. However, Calcein-AM was able to visualize cells clearly when added to both the inner and outer wells. However, the fluorescent signal was inconsistent and partially washed out at the 10, 60, and 120 minute time points. Based on these results, the optimal method for imaging unlabeled cells is to incubate each sample for 30 minutes with 1 μM Calcein-AM added to both the inner and outer wells.

5.6 Future perspectives

With the potential for expansion into unlabeled cell lines, a generalized experimental structure can be created based on the results of labelled cells within the SISser model. After selection of a cohort of cells to analyze, varying concentrations of cells may be seeded and followed visually with confocal microscopy to determine optimal seeding concentrations to allow for a common time endpoint to be established. If material availability is limited, endpoints based on cell volume or confluency may be determined before seeding, with each condition halted upon reaching the desired threshold. Consistent endpoints ensure that analyzed information across multiple conditions can be reliably compared.

Another potentially useful area of expansion for SISser models is with the application of additional cell types in coculture. For example, immune cells such as macrophages have been shown to play an integral role in the development of PDAC (26), and inclusion of these samples in coculture with pancreatic cells and fibroblasts may result in more biologically relevant cell interactions. Endothelial cells are also commonly found in the tumor microenvironment, interacting with and directing immune cells as well (88). With the addition of each cell type in coculture, it would certainly be interesting to analyze if cell interactions seen in PDAC are conserved in our system.

Decellularized porcine intestinal scaffold models also possess the ability to mimic vascularization. Intestinal samples may be processed in a manner retaining the vascular system, which may then be attached to a bioreactor to provide accurate vascular flow (70). Given the importance of vascularity in both drug delivery and tumor progression (89), dynamic models with vascularization provide a much more accurate biological context compared to similar models in static conditions.

More accurate analysis and characterization of the SISser model would also prove beneficial moving forward. In the current experiments, analysis was primarily based on morphology, focusing on areas such as the concentration and location of cells. While this information is useful in understanding cell behavior, more accurate characterization would be useful to gather more detailed information on the state of cells within the model. For example, immunohistochemistry may be employed to accurately label ECM factors typically secreted by PSCs (24) to determine if the interaction observed between fibroblasts and pancreatic cells is representative of that seen in PDAC. Also, PDAC tumor progression may be characterized by marker expression, providing the ability to assess the similarity of activity of cells within the model compared to examples seen in PDAC (90). Combination with flow cytometry would provide an opportunity to assess expression patterns of the pancreatic cells under various conditions. This method may provide information on the activity and expression of cells as they interact with the scaffold, for example if there are some differences between cells located in the oval-shaped colonies as opposed to those that seem to travel independently from the surface. Also, characterization of expression patterns may provide some insight into the different responses of BxPC-3 cells.

One goal in the development of a SISser model is the ability to accurately predict tumor response to various therapeutic strategies. With the addition of prevalent PDAC treatments, such as nab-paclitaxel + gemcitabine or FOLFIRINOX, the response of cells within the SISser model can be compared to responses generated in other model systems, such as orthotopic injection, as well as primary tumors. Given the ability for permeation seen in the SISser scaffold (Fig 4.2c), it would be interesting to assess the treatment effects when the drug must travel through the matrix.

Ultimately, the SISser model system applied to PDAC shows potential in filling a necessary preclinical niche, retaining the efficiency of an *in vitro* model while providing accurate and biologically representative development typically reserved for *in vivo* models.

References

1. Siegel, R.L., K.D. Miller, and A. Jemal, *Cancer statistics, 2019.* CA: A Cancer Journal for Clinicians, 2019. **69**(1): p. 7-34.
2. Bekkali, N.L.H. and K.W. Oppong, *Pancreatic ductal adenocarcinoma epidemiology and risk assessment: Could we prevent? Possibility for an early diagnosis.* Endoscopic ultrasound, 2017. **6**(Suppl 3): p. S58-S61.
3. Chari, S.T., et al., *Early detection of sporadic pancreatic cancer: summative review.* Pancreas, 2015. **44**(5): p. 693-712.
4. Hidalgo, M., *Pancreatic Cancer.* New England Journal of Medicine, 2010. **362**(17): p. 1605-1617.
5. Brune, K., et al., *Multifocal neoplastic precursor lesions associated with lobular atrophy of the pancreas in patients having a strong family history of pancreatic cancer.* The American journal of surgical pathology, 2006. **30**(9): p. 1067-1076.
6. Basturk, O., et al., *A Revised Classification System and Recommendations From the Baltimore Consensus Meeting for Neoplastic Precursor Lesions in the Pancreas.* The American journal of surgical pathology, 2015. **39**(12): p. 1730-1741.
7. Hruban, R.H., A. Maitra, and M. Goggins, *Update on pancreatic intraepithelial neoplasia.* International journal of clinical and experimental pathology, 2008. **1**(4): p. 306-316.
8. Yachida, S., et al., *Distant metastasis occurs late during the genetic evolution of pancreatic cancer.* Nature, 2010. **467**(7319): p. 1114-1117.
9. Yu, J., et al., *Time to progression of pancreatic ductal adenocarcinoma from low-to-high tumour stages.* Gut, 2015. **64**(11): p. 1783-1789.
10. McWilliams, R.R., et al., *Risk of malignancy in first-degree relatives of patients with pancreatic carcinoma.* Cancer, 2005. **104**(2): p. 388-394.
11. Maitra, A. and R.H. Hruban, *Pancreatic Cancer.* Annual Review of Pathology: Mechanisms of Disease, 2008. **3**(1): p. 157-188.
12. Sohn, T.A., et al., *Resected adenocarcinoma of the pancreas—616 patients: results, outcomes, and prognostic indicators.* Journal of Gastrointestinal Surgery, 2000. **4**(6): p. 567-579.
13. Katz, M.H.G., et al., *Tumor-Node-Metastasis Staging of Pancreatic Adenocarcinoma.* CA: A Cancer Journal for Clinicians, 2008. **58**(2): p. 111-125.
14. Burris, H.A., et al., *Improvements in survival and clinical benefit with gemcitabine as first-line therapy for patients with advanced pancreas cancer: a randomized trial.* Journal of Clinical Oncology, 1997. **15**(6): p. 2403-2413.
15. Conroy, T., et al., *FOLFIRINOX versus Gemcitabine for Metastatic Pancreatic Cancer.* New England Journal of Medicine, 2011. **364**(19): p. 1817-1825.
16. Von Hoff, D.D., et al., *Increased Survival in Pancreatic Cancer with nab-Paclitaxel plus Gemcitabine.* New England Journal of Medicine, 2013. **369**(18): p. 1691-1703.
17. Ellenrieder, V., A. König, and T. Seufferlein, *Current Standard and Future Perspectives in First- and Second-Line Treatment of Metastatic Pancreatic Adenocarcinoma.* Digestion, 2016. **94**(1): p. 44-49.
18. Oberstein, P.E. and K.P. Olive, *Pancreatic cancer: why is it so hard to treat?* Therapeutic advances in gastroenterology, 2013. **6**(4): p. 321-337.

19. Mahadevan, D. and D.D. Von Hoff, *Tumor-stroma interactions in pancreatic ductal adenocarcinoma.* Molecular Cancer Therapeutics, 2007. **6**(4): p. 1186.
20. Dauer, P., et al., *Microenvironment in determining chemo-resistance in pancreatic cancer: Neighborhood matters.* Pancreatology : official journal of the International Association of Pancreatology (IAP) ... [et al.], 2017. **17**(1): p. 7-12.
21. Korc, M., *Pancreatic cancer-associated stroma production.* American journal of surgery, 2007. **194**(4 Suppl): p. S84-S86.
22. Liang, C., et al., *Complex roles of the stroma in the intrinsic resistance to gemcitabine in pancreatic cancer: where we are and where we are going.* Experimental &Amp; Molecular Medicine, 2017. **49**: p. e406.
23. Bachem, M.G., et al., *Pancreatic carcinoma cells induce fibrosis by stimulating proliferation and matrix synthesis of stellate cells.* Gastroenterology, 2005. **128**(4): p. 907-921.
24. Özdemir, B.C., et al., *Depletion of carcinoma-associated fibroblasts and fibrosis induces immunosuppression and accelerates pancreas cancer with reduced survival.* Cancer cell, 2014. **25**(6): p. 719-734.
25. Hwang, R.F., et al., *Cancer-associated stromal fibroblasts promote pancreatic tumor progression.* Cancer research, 2008. **68**(3): p. 918-926.
26. Froeling, F.E.M., et al., *Retinoic Acid–Induced Pancreatic Stellate Cell Quiescence Reduces Paracrine Wnt–β-Catenin Signaling to Slow Tumor Progression.* Gastroenterology, 2011. **141**(4): p. 1486-1497.e14.
27. Liu, Y. and X. Cao, *The origin and function of tumor-associated macrophages.* Cellular & molecular immunology, 2015. **12**(1): p. 1-4.
28. Ye, H., et al., *Tumor-associated macrophages promote progression and the Warburg effect via CCL18/NF-kB/VCAM-1 pathway in pancreatic ductal adenocarcinoma.* Cell death & disease, 2018. **9**(5): p. 453-453.
29. Makareeva, E., et al., *Carcinomas contain a matrix metalloproteinase-resistant isoform of type I collagen exerting selective support to invasion.* Cancer research, 2010. **70**(11): p. 4366-4374.
30. Yilmaz, M. and G. Christofori, *EMT, the cytoskeleton, and cancer cell invasion.* Cancer and Metastasis Reviews, 2009. **28**(1): p. 15-33.
31. Toole, B.P., *Hyaluronan: from extracellular glue to pericellular cue.* Nature Reviews Cancer, 2004. **4**(7): p. 528-539.
32. Sato, N., et al., *Role of hyaluronan in pancreatic cancer biology and therapy: Once again in the spotlight.* Cancer science, 2016. **107**(5): p. 569-575.
33. Misra, S., et al., *Hyaluronan-CD44 interactions as potential targets for cancer therapy.* The FEBS journal, 2011. **278**(9): p. 1429-1443.
34. Cheng, X.-B., et al., *Receptor for Hyaluronic Acid-Mediated Motility is Associated with Poor Survival in Pancreatic Ductal Adenocarcinoma.* Journal of Cancer, 2015. **6**(11): p. 1093-1098.
35. Chen, J., et al., *Overexpression of α3, β3 and γ2 chains of laminin-332 is associated with poor prognosis in pancreatic ductal adenocarcinoma.* Oncology letters, 2018. **16**(1): p. 199-210.
36. Charrier, A. and D.R. Brigstock, *Regulation of pancreatic function by connective tissue growth factor (CTGF, CCN2).* Cytokine & growth factor reviews, 2013. **24**(1): p. 59-68.

37. Tang, D., et al., *Persistent activation of pancreatic stellate cells creates a microenvironment favorable for the malignant behavior of pancreatic ductal adenocarcinoma.* International Journal of Cancer, 2013. **132**(5): p. 993-1003.
38. Deer, E.L., et al., *Phenotype and genotype of pancreatic cancer cell lines.* Pancreas, 2010. **39**(4): p. 425-435.
39. Henderson, M.C., et al., *High-throughput RNAi screening identifies a role for TNK1 in growth and survival of pancreatic cancer cells.* Molecular cancer research : MCR, 2011. **9**(6): p. 724-732.
40. Bachem, M.G., et al., *Pancreatic stellate cells—role in pancreas cancer.* Langenbeck's Archives of Surgery, 2008. **393**(6): p. 891-900.
41. Hwang, R.F., et al., *Cancer-Associated Stromal Fibroblasts Promote Pancreatic Tumor Progression.* Cancer Research, 2008. **68**(3): p. 918.
42. Kim, I., et al., *A drug-repositioning screen for primary pancreatic ductal adenocarcinoma cells identifies 6-thioguanine as an effective therapeutic agent for TPMT-low cancer cells.* Molecular oncology, 2018. **12**(9): p. 1526-1539.
43. Collisson, E.A., et al., *Subtypes of pancreatic ductal adenocarcinoma and their differing responses to therapy.* Nature medicine, 2011. **17**(4): p. 500-503.
44. Froeling, F.E.M., J.F. Marshall, and H.M. Kocher, *Pancreatic cancer organotypic cultures.* Journal of Biotechnology, 2010. **148**(1): p. 16-23.
45. Gadaleta, E., et al., *A global insight into a cancer transcriptional space using pancreatic data: importance, findings and flaws.* Nucleic acids research, 2011. **39**(18): p. 7900-7907.
46. Kim, M.P., et al., *Generation of orthotopic and heterotopic human pancreatic cancer xenografts in immunodeficient mice.* Nature protocols, 2009. **4**(11): p. 1670-1680.
47. Garber, K., *From Human to Mouse and Back: "Tumorgraft" Models Surge in Popularity.* JNCI: Journal of the National Cancer Institute, 2009. **101**(1): p. 6-8.
48. Hwang, C.-I., et al., *Preclinical models of pancreatic ductal adenocarcinoma.* The Journal of pathology, 2016. **238**(2): p. 197-204.
49. Garrido-Laguna, I., et al., *Tumor Engraftment in Nude Mice and Enrichment in Stroma-Related Gene Pathways Predict Poor Survival and Resistance to Gemcitabine in Patients with Pancreatic Cancer.* Clinical Cancer Research, 2011. **17**(17): p. 5793.
50. Bian, B., et al., *Gene expression profiling of patient-derived pancreatic cancer xenografts predicts sensitivity to the BET bromodomain inhibitor JQ1: implications for individualized medicine efforts.* EMBO Molecular Medicine, 2017. **9**(4): p. 482.
51. Yapp, D.T., et al., *The differential effects of metronomic gemcitabine and antiangiogenic treatment in patient-derived xenografts of pancreatic cancer: treatment effects on metabolism, vascular function, cell proliferation, and tumor growth.* Angiogenesis, 2016. **19**(2): p. 229-244.
52. Kawaguchi, K., et al., *MEK inhibitors cobimetinib and trametinib, regressed a gemcitabine-resistant pancreatic-cancer patient-derived orthotopic xenograft (PDOX).* Oncotarget, 2017. **8**(29): p. 47490-47496.
53. Ryan, D.P., T.S. Hong, and N. Bardeesy, *Pancreatic Adenocarcinoma.* New England Journal of Medicine, 2014. **371**(11): p. 1039-1049.

54. Allaway, R.J., et al., *Genomic characterization of patient-derived xenograft models established from fine needle aspirate biopsies of a primary pancreatic ductal adenocarcinoma and from patient-matched metastatic sites.* Oncotarget, 2016. **7**(13): p. 17087-17102.
55. Sereti, E., et al., *Patient Derived Xenografts (PDX) for personalized treatment of pancreatic cancer: emerging allies in the war on a devastating cancer?* Journal of Proteomics, 2018. **188**: p. 107-118.
56. Tentler, J.J., et al., *Patient-derived tumour xenografts as models for oncology drug development.* Nature reviews. Clinical oncology, 2012. **9**(6): p. 338-350.
57. Baker, L.A., et al., *Modeling pancreatic cancer with organoids.* Trends in cancer, 2016. **2**(4): p. 176-190.
58. Huang, L., et al., *Ductal pancreatic cancer modeling and drug screening using human pluripotent stem cell- and patient-derived tumor organoids.* Nature medicine, 2015. **21**(11): p. 1364-1371.
59. Boj, S.F., et al., *Organoid models of human and mouse ductal pancreatic cancer.* Cell, 2015. **160**(1-2): p. 324-338.
60. Longati, P., et al., *3D pancreatic carcinoma spheroids induce a matrix-rich, chemoresistant phenotype offering a better model for drug testing.* BMC cancer, 2013. **13**: p. 95-95.
61. Walsh, A.J., R.S. Cook, and M.C. Skala, *Functional Optical Imaging of Primary Human Tumor Organoids: Development of a Personalized Drug Screen.* Journal of Nuclear Medicine, 2017. **58**(9): p. 1367-1372.
62. Thiele, J., et al., *25th Anniversary Article: Designer Hydrogels for Cell Cultures: A Materials Selection Guide.* Advanced Materials, 2014. **26**(1): p. 125-148.
63. Saez, A., et al., *Rigidity-driven growth and migration of epithelial cells on microstructured anisotropic substrates.* Proceedings of the National Academy of Sciences of the United States of America, 2007. **104**(20): p. 8281-8286.
64. Lutolf, M.P., et al., *Cell-Responsive Synthetic Hydrogels.* Advanced Materials, 2003. **15**(11): p. 888-892.
65. Barbarisi, M., et al., *Use of polycaprolactone (PCL) as scaffolds for the regeneration of nerve tissue.* Journal of Biomedical Materials Research Part A, 2015. **103**(5): p. 1755-1760.
66. Lukashev, M.E. and Z. Werb, *ECM signalling: orchestrating cell behaviour and misbehaviour.* Trends in Cell Biology, 1998. **8**(11): p. 437-441.
67. Shaheen, N.L., et al., *Extracellular matrix composition modulates angiosarcoma cell attachment and proliferation.* Oncoscience, 2017. **4**(11-12): p. 178-188.
68. Nietzer, S., et al., *Mimicking Metastases Including Tumor Stroma: A New Technique to Generate a Three-Dimensional Colorectal Cancer Model Based on a Biological Decellularized Intestinal Scaffold.* Tissue engineering. Part C, Methods, 2016. **22**(7): p. 621-635.
69. Badylak, S., et al., *Small intestinal submucosa: A substrate for in vitro cell growth*. Vol. 9. 1998. 863-78.
70. Schanz, J., et al., *Vascularised human tissue models: A new approach for the refinement of biomedical research.* Journal of Biotechnology, 2010. **148**(1): p. 56-63.
71. Ferreira, L.P., V.M. Gaspar, and J.F. Mano, *Design of spherically structured 3D in vitro tumor models -Advances and prospects.* Acta Biomaterialia, 2018. **75**: p. 11-34.

72. Stratmann, A.T., et al., *Establishment of a human 3D lung cancer model based on a biological tissue matrix combined with a Boolean in silico model.* Molecular oncology, 2014. **8**(2): p. 351-365.
73. Schuerlein, S., et al., *A versatile modular bioreactor platform for Tissue Engineering.* Biotechnology journal, 2017. **12**(2): p. 1600326.
74. Jonkman, J. and C.M. Brown, *Any Way You Slice It-A Comparison of Confocal Microscopy Techniques.* Journal of biomolecular techniques : JBT, 2015. **26**(2): p. 54-65.
75. Yoshida, E., et al., *In vivo wide-field calcium imaging of mouse thalamocortical synapses with an 8 K ultra-high-definition camera*. Vol. 8. 2018.
76. Choy, G., P. Choyke, and S.K. Libutti, *Current Advances in Molecular Imaging: Noninvasive in Vivo Bioluminescent and Fluorescent Optical Imaging in Cancer Research.* Molecular Imaging, 2003. **2**(4): p. 15353500200303142.
77. Troy, T., et al., *Quantitative Comparison of the Sensitivity of Detection of Fluorescent and Bioluminescent Reporters in Animal Models.* Molecular Imaging, 2004. **3**(1): p. 15353500200403196.
78. Searle, P.F., et al., *NITROREDUCTASE: A PRODRUG-ACTIVATING ENZYME FOR CANCER GENE THERAPY.* Clinical and Experimental Pharmacology and Physiology, 2004. **31**(11): p. 811-816.
79. Sharma, K., K. Sengupta, and H. Chakrapani, *Nitroreductase-activated nitric oxide (NO) prodrugs.* Bioorganic & Medicinal Chemistry Letters, 2013. **23**(21): p. 5964-5967.
80. McCormack, E., et al., *Nitroreductase, a Near-Infrared Reporter Platform for In Vivo Time-Domain Optical Imaging of Metastatic Cancer.* Cancer Research, 2013. **73**(4): p. 1276.
81. Miles, F.L., J.E. Lynch, and R.A. Sikes, *Cell-based assays using calcein acetoxymethyl ester show variation in fluorescence with treatment conditions.* Journal of biological methods, 2015. **2**(3): p. e29.
82. Bankhead, P., et al., *QuPath: Open source software for digital pathology image analysis.* Scientific Reports, 2017. **7**(1): p. 16878.
83. Katzer, A., et al., *Polyetheretherketone—cytotoxicity and mutagenicity in vitro.* Biomaterials, 2002. **23**(8): p. 1749-1759.
84. Loukopoulos, P., et al., *Orthotopic Transplantation Models of Pancreatic Adenocarcinoma Derived From Cell Lines and Primary Tumors and Displaying Varying Metastatic Activity.* Pancreas, 2004. **29**(3).
85. Avci, P., et al., *Low-level laser (light) therapy (LLLT) in skin: stimulating, healing, restoring.* Seminars in cutaneous medicine and surgery, 2013. **32**(1): p. 41-52.
86. Funahashi, H., et al., *Alteration of Integrin Expression by Glial Cell Line-Derived Neurotrophic Factor (GDNF) in Human Pancreatic Cancer Cells.* Pancreas, 2003. **27**(2).
87. Zhang, J., et al., *Efficient Two-Photon Fluorescent Probe for Nitroreductase Detection and Hypoxia Imaging in Tumor Cells and Tissues.* Analytical Chemistry, 2015. **87**(23): p. 11832-11839.
88. Dougan, S.K., *The Pancreatic Cancer Microenvironment.* The Cancer Journal, 2017. **23**(6).
89. Azzi, S., J.K. Hebda, and J. Gavard, *Vascular permeability and drug delivery in cancers.* Frontiers in oncology, 2013. **3**: p. 211-211.

90. Ferreira, R.M.M., et al., *Duct- and Acinar-Derived Pancreatic Ductal Adenocarcinomas Show Distinct Tumor Progression and Marker Expression.* Cell reports, 2017. **21**(4): p. 966-978.